Fine-tune the electronic structure in Co-Mo based catalysts to give easily coupled HER and OER catalysts for effective water splitting

Xinhui Zhang, Aiping Wu [*], Dongxu Wang, Yanqing Jiao, Haijing Yan, Chengxu Jin, Ying Xie [*], Chungui Tian [*]

Key Laboratory of Functional Inorganic Material Chemistry, Ministry of Education of the People's Republic of China, Heilongjiang University, Harbin Xuefu Road, 150080, PR China

ABSTRACT

The easily coupled HER and OER catalysts are highly desired for the hydrogen evolution by overall water splitting. Here, we design and synthesize Co-Mo based catalysts with adjustable electronic structure by tuning the Mo/Co ratio to give easily coupled, effective HER/OER catalysts. At lower Mo/Co ratio, the Mo component can move up the d-band center of the catalysts, rendering an enhanced capability of activating H_2O to improve OER performance with a low overpotential of 223 mV at 10 mA cm^{-2} (η_{10}). Contrastingly, the Co component in the catalyst with higher Mo/Co ratio can induce the downward shift of the d-band center, optimizing the Gibbs free energy of hydrogen adsorption to enhance the HER activity (a low η_{10} of 52 mV). These HER and OER catalysts with similar components can be coupled for overall water splitting. The electrolyzer can be driven by a solar panel to achieve effective H_2 production.

1. Introduction

Hydrogen is considered as a green energy carrier because of its high energy density and environmental friendliness [1–4]. Electrocatalytic water splitting, driven by low voltage electricity converted from solar energy and wind energy, is the most promising way to produce H_2 cleanly [5–7]. The replacement of the noble metal catalysts (Pt and RuO_2 etc.) for saving the cost is focus in the area [8–11]. Recent years have witnessed the progress in designing the HER and OER catalysts by the size control, hetero-atom doping and morphology adjustment [12–15]. Notably, the water splitting requires the coupling of effective HER and OER catalysts. Some bi-functional catalysts can only effectively work for a certain half-reaction, thus showing a low activity for overall water splitting [16,17]; while the combination of good HER/OER catalysts with different compositions will bring difficulty in the preparation and matching [18]. Therefore, the construction of easily matched, effective HER/OER catalysts is of great significance for the efficient overall water splitting.

Transition metal interstitial compound (TMICs) are promising catalysts in water electrolysis. TMICs hold novel characteristics in their Pt-like electronic structure, high electronic conductivity, excellent mechanical and chemical stability, and good corrosion resistance, which render them with a high electrocatalytic activity toward effectively catalyze HER/OER [19–22]. Studies have shown that the early transition metal interstitial compound (ETMICs, Mo_2C, WC etc.) can trap and activate protons for catalyzing HER [23–25]. However, the late TMICs (LTMICs, CoP, NiP etc.) can act as bi-functional catalysts for OER/HER, but suffered from low activity for overall water splitting due to the moderate activity for one half reaction or both reaction [26,27]. Moreover, the tune of the electronic structure is of important for giving optimized catalysts [28–31]. In this regard, the combination of ETMs and LTMs can optimize the electronic structure for enhancing HER/OER performance due to "d-electron compensation effect". By rationalizing the components and micro-structure, the bi-metallic TMICs (BTIMCs) with enhanced HER activity have been obtained, including $Ni_3Mo_3C@NPC$ NWs/CC (η_{100} of 215 mV) [32], $NiMo_2C@C$ (η_{10} of 169 mV) in 1.0 M KOH [33]. Also, the BTIMCs can catalyze OER due to the LTMs in the catalysts are active pre-catalysts for OER, such as Mo_6Ni_6C (η_{10} of 190 mV) [34], Co_3ZnC/Co (η_{10} of 366 mV) [35], $Co_6Mo_6C_2/NCRGO$ (η_{10} of 260 mV) in 1.0 M KOH [36]. Therefore, the BTIMCs can act as bi-functional catalysts for HER/OER. For example, the $Co_6W_6C@NC$ gives good HER performance (η_{10} of 59 mV) and OER performance (η_{10} of 286 mV) [37]. The W-Cu based BTIMCs displayed η_{10} of 238 mV for OER and 98 mV for HER [38]. Nevertheless, the

---

BTMCs have still only faced with a good performance for certain half-reaction, thus showing a low activity for overall water splitting. For example, the $Co_6W_6C@NC\|Co_6W_6C@NC$ electrodes need a large cell voltage of 1.585 V to obtain the current density of 10 mA cm^{-2} [37]. Therefore, it is necessary to adjust the electronic structure on a wide scale so as to make effective and easily coupled HER and OER catalysts with the same components, which is very beneficial to the construction of overall water splitting system, but study about this is seldom.

Generally, the TMICs are formed by the heating treatment of the corresponding bi-metal precursor [39,40]. So, the design of the precursors with tunable metal ratios is precondition to synthesize matched OER/HER catalysts. Here, we have reported a robust method to construct the bi-metal TMICs with tunable ratios of ETMs and LTMs. The precursor is from the assembly of ZIF-67 cube and phosphomolybdic acid ($[PMo_{12}O_{40}]^{3-}$, PMo_{12}). The pore size of ZIF-67 matches the size of $[PMo_{12}O_{40}]^{3-}$ (PMo_{12}) clusters, providing an opportunity for the combination of Co with different amount of Mo. Our results indicate that the catalysts with low Mo/Co ratio have a solid structure, and are suitable for OER, while the catalysts with high Mo/Co ratio have hollow structure and are suitable for HER. In 1.0 M KOH electrolyte, the optimized catalyst only requires low overpotentials of 223 and 52 mV to reach 10 mA cm^{-2} for OER and HER, respectively. The electrolytic cell assembled with two catalysts needs only 1.53 V to afford 10 mA cm^{-2}. Our previous work shows the preparation of solid Mo_3Co_3C/Mo_6Co_6C polyhedral catalyst based on the "trapping" of PMo_{12} in a dodecahedral ZIF-67, which needs 1.61 V to afford 10 mA cm^{-2} for overall water splitting [41]. Our present work verified that the morphology (exposed plane) of ZIF-67 can affect the structure of final catalysts.

2. Experimental section

2.1. Materials

Cobalt nitrate hexahydrate ($Co(NO_3)_2·6H_2O$, 99 wt%) and 2-methylimidazole ($C_4H_6N_2$, 98%) were obtained from Aladdin Ltd. Phosphomolybdic acid hydrate ($H_3Mo_{12}O_{40}P·xH_2O$, ≥99.9 wt%) was purchased from Sinopharm Chemical Reagent Co., Ltd. Cetyltrimethylammonium bromide ($C_{19}H_{42}BrN$, ≥99.0%) was purchased from Tianjin Guangfu Fine Chemical Research Institute. Methanol (CH_3OH, ≥99.5 wt%) and ethanol (CH_3CH_2OH, ≥99.7 wt%) was purchased from Tianjin Fuyu Fine Chemical Co., Ltd. Pt/C (20%) was obtained from Shanghai Hesen Electric Corporation. RuO_2 was purchased from Aladdin Ltd. There was no further purification of all the reagents and solvents.

2.2. Synthesis of ZIF-67

The ZIF-67 nanocubes were synthesized according to the previous report [42,43]. Specifically, 58 mg of $Co(NO_3)_2·6H_2O$ was dissolved in 2 mL of deionized water (DIW) containing 1 mg of cetyltrimethylammonium bromide (CTAB). The above solution was then rapidly injected into 14 mL of an aqueous solution containing 908 mg of 2-methyimidazole (2-MIM), and stirred at room temperature for 20 min. Lastly, the product was collected by centrifugation, washed with ethanol several times.

2.3. Synthesis of Co-Mo-X

The Co-Mo-*X* was obtained through the following procedure. 0.1 g of ZIF-67 was dispersed in 30 mL of methanol and stirred at room temperature for 4 h (solution A). A certain amount of $H_3PMo_{12}O_{40}$ (*X* = 0.005 g, 0.025 g, 0.05 g, 0.06 g, 0.07 g, 0.1 g, 0.11 g, 0.125 g) was dissolved in 30 mL of methanol (solution B). Solution B was quickly poured into solution A under constant stirring. The mixture was stirred for 30 min and then transferred into a 100 mL Teflonlined autoclave. Subsequently, the autoclave was sealed and maintained at 85 ℃ for 4 h. The resulting solid was collected and washed with methanol at least

three times and then dried at 60 ℃ in a vacuum oven for 12 h. The obtained product was denoted Co-Mo-*X*, where *X* represented the addition amount of PMo_{12} in the synthesis process.

2.4. Synthesis of Co-Mo-X-yN

In a typical procedure, Co-Mo-*X* was placed in a porcelain boat. The boat was heated from room temperature to 600 ℃ at a rate of 2 ℃ min^{-1} and held at 600 ℃ for 0.5 h under a N_2 atmosphere. After natural cooling down to room temperature, the electrocatalyst was obtained and marked as Co-Mo-*X*-6N (6N representing calcination at 600 ℃ under N_2). The Co-Mo-0.005 and Co-Mo-0.125 were also calcined at 500 and 700 ℃ under a N_2 atmosphere, respectively, to tune the components and micro-structures. The corresponding samples were named Co-Mo-0.005–5N, Co-Mo-0.005–7N, Co-Mo-0.125–5N and Co-Mo-0.125–7N, respectively. For comparison, Table S1 lists the information of the obtained samples.

2.5. Structural characterization

X-ray diffraction (XRD) patterns were recorded in the 2θ range of 10–80° on a Bruker D8 Advance X-ray diffractometer with CuKα (λ = 1.5418 Å) radiation (40 kV, 40 mA), and a Rigaku D/max-2600/PC X-ray diffractometer (XRD, Cu-Kα radiation). Scanning electron microscopy (SEM) test was carried out on a Hitachi S-4800 instrument at an accelerating voltage of 5 kV. The transmission electron microscopy (TEM) and high resolution TEM (HRTEM) was performed on a JEM-F200 electron microscope (JEOL, Japan) with an acceleration voltage of 200 kV. X-ray photon spectroscopy (XPS) analysis was performed using a VG ESCALABMK II with Mg-Ka radiation (1253.6 eV). Thermogravimetric (TG) analysis was obtained on a SDT Q600 instrument with a constant flow of air. A PE Spectrum One B IR spectrometer was used to record the fourier transform infrared spectra (FT-IR) of the samples in the region 400–4000 cm^{-1} with KBr pellets. Nitrogen adsorption-desorption isotherms were measured at 77 K on a Quantachrome autosorb iQ/ASiQwin. The Brunauer–Emmett–Teller method was used to calculate the specific surface area. Scanning Kelvin Probe (SKP) measurements (SKP5050 system, Scotland) were made in ambient atmosphere, and a gold electrode was used as the reference electrode. The work function (φ) was calculated by using the formula.

$$\varphi_{Au} - \eta_{Au}/1000 = \varphi - \eta/1000$$

in which φAu is the work function of Au and $\eta_{Au} = -239.75$ eV.

2.6. Electrochemical measurements

All electrochemical measurements were carried out on a CHI 760E electrochemical workstation in a typical three-electrode configuration at room temperature. In 1 M KOH, an Hg/HgO electrode and a graphite rod were used as the reference electrode and counter electrodes, respectively. The working electrode was prepared by mixing 5 mg of sample, 1 mg carbon black and 30 μL Nafion (5 wt%) were dispersed in a mixture of water and ethanol (v: v = 1: 1). The mixture was treated to obtain a homogeneous ink. Subsequently, the catalyst ink was smeared onto Ni foam (1 cm × 1 cm). The Ni foam coated with the sample was dried at 60 ℃ for 12 h in a vacuum oven. Before coating, the NF was washed with acetone, HCl aqueous solution (2 M), deionized water and ethanol in sequence. The linear sweep voltammograms (LSV) test was carried out in 1 M KOH with the scan rate of 5 mV s^{-1}, which was performed after 20 cycles of cyclic voltammetry (CV) tests to steady the current. In all measurements, the final potentials were calibrated to reversible hydrogen electrode (RHE) based on the Nernst equation: $E_{RHE} = E_{Hg/HgO} + 0.059 × pH + E^{\theta}_{Hg/HgO}$. The Tafel plots were derived from polarization curves. Cyclic voltammetry (CV) was carried out at scan rates from 10 to 100 mV s^{-1} to estimate the electrochemical double layer capacitance

(C$_{dl}$). Using the IR compensation function of CHI-760E electrochemical workstation, the LSV data of a typical catalyst with 90% IR compensation was obtained. The electrochemical impedance spectroscopy (EIS) was performed from the LSV curve at a corresponding potential of 10 mA cm^{-2}, and the frequency range was 0.01–100000 Hz. Under a static overpotential, the electrochemical stability is evaluated by measuring the change of current with time by chronoamperometry. The ECSA is the electrochemically active surface area, which can be calculated by the following formula:

$$ECSA = \frac{specific\ capacitance}{40\ \mu F\ cm^{-2}\ per\ cm^2}$$

where specific capacitance is Cdl, and 40 μF cm^{-2} is a constant to convert capacitance to ECSA. Using the specific capacitance value of a plane standard with an actual surface area of 1 cm^2, the specific capacitance can be converted into an electrochemically active surface area (ECSA).

The Faradaic efficiency (FE) of the catalyst was obtained by comparing the measured gas amount during electrolysis with the theoretical gas amount. In a closed h-shaped electrolytic cell, constant potential electrolysis was performed at 90 mA cm^{-2} for 60 min to complete the separate H$_2$/O$_2$ gas collection that was quantitatively evaluated by drainage method. The theoretical H$_2$ amount was calculated as follows:

$$n(H_2) = \frac{Q}{nF}$$

where Q was the charge passed through the electrodes, n(H$_2$) was the number of moles of hydrogen produced, F was the faradaic constant (96,485 C mol^{-1}), and n was the number of electrons transferred during water splitting (for HER, n was 2). The calculation of the theoretical amount of O$_2$ was the same as that for H$_2$ except n = 4.

Turnover frequency (TOF) was calculated by supposing every corresponding metal atom as active sites involved with catalytic reaction, showing as equation:

$$TOF = \frac{jS}{zFn}$$

where *j* is measured current density (mA cm^{-2}); S is geometrical surface area of working electrode (1 cm^{-2}); z is electron transfer number per molecule generated O$_2$/H$_2$ (z = 4 for OER, z = 2 for HER); F is Faraday's constant (96,485.3 C mol^{-1}), and n is the moles of the corresponding metal atom (mol) within the catalyst loading.

2.7. Theoretical calculation

Density Functional Theory (DFT) simulations were performed by employing Cambridge Sequential Total Energy Package (CASTEP) module implemented in Material Studio. The generalized gradient approximation (GGA) with a Perdew-Burke-Ernzerhof (PBE) functional was used to describe the electronic exchange and correlation effects, and the kinetic energy cutoff was set to be 340 eV. The self-consistent field (SCF) tolerance was 1×10^{-6} eV and Monkhorst-Pack mesh of $3 \times 3 \times 1$ was used to perform geometry optimization. The adsorption free energies of H (ΔG_{H*}) is usually considered as an effective descriptor for HER activity and a catalyst with $\Delta G_{H*} = 0$ can be an excellent candidate for HER. The Gibbs free-energy of H* (ΔG_{H*}) can be calculated by the equation $\Delta G_{H*} = \Delta E_{H*} + \Delta E_{ZPE} - T\Delta S$, where ΔE_{H*}, ΔE_{ZPE} and ΔS are the adsorption energy of atomic hydrogens on the given unit cell, the difference corresponding to the zero point energy between the adsorbed hydrogen and hydrogen in the gas phase and the entropy change of H* adsorption, respectively. ΔS can be obtained by $\Delta S = S$ (H*) - $1/2S_{0\ H2}$ ($S_{0\ H2}$ is the entropy of H$_2$ in the gas phase at standard conditions). As the entropy of hydrogen in absorbed state is negligible, ΔS can be calculated as $-1/2S_{0\ H2}$. Therefore, the Gibbs free energy of

H* can be taken as: $\Delta G_{H*} = \Delta E_{H*} + 0.24$ eV.

3. Results and discussion

### 3.1. Structural characterization of Co-Mo based catalysts

We aim to prepare Co-Mo based BTMCs with different Co/Mo ratios (Table S1), in which the ZIF-67 was selected as the morphological template and Co source, and PMo$_{12}$ as the Mo source. As shown in Fig. 1, the uniform ZIF-67 nanocubes are firstly prepared. Then, the PMo$_{12}$ with adjustable amount was trapped into cubic ZIF-67, resulting in the formation of PMo$_{12}$/ZIF-67 precursors. In this step, the Mo/Co ratio in PMo$_{12}$/ZIF-67 can be broadly tuned (from about 30:1–1:1). Notably, the change of Mo/Co ratio in PMo$_{12}$/ZIF-67 precursor can tune the structure of precursor as solid cubes (low Mo/Co ratio) and hollow cubes (high Mo/Co ratio). A controlled pyrolysis can transform the PMo$_{12}$/ZIF-67 into Co$_6$Mo$_6$C/MoC/Co bimetallic carbides with different Co/Mo ratios and solid or hollow structures. The tunability of Mo/Co ratio and morphology of the BTMCs provides an opportunity to tune the electrocatalytic performance.

A series of characterizations show the successful combination of ZIF-67 cubes with different amount of PMo$_{12}$. As shown in Fig. 2a and Fig. S1, the Co-Mo-0.005 and Co-Mo-0.125 precursors show the identical X-ray diffraction (XRD) patterns with those of ZIF-67, indicating that the introduction of PMo$_{12}$ clusters does not change the crystal parameters of ZIF-67. Thermogravimetric (TG) testing of the two precursors further shows the access of PMo$_{12}$ into ZIF-67 (Fig. S2). The lower value of weight loss for Co-Mo-0.005 than Co-Mo-0.125 proves the adjustable trapping of PMo$_{12}$ into ZIF-67. ICP tests show that the Co/Mo ratio in Co-Mo-0.005 and Co-Mo-0.125 precursor are about 30:1 and 1:1, respectively (Table S2). A series of characterizations (IR, XPS and EDX spectrum) further confirmed the restrictions of PMo$_{12}$ by the ZIF-67 (Figs. S3-S6). The above results indicated the successful combination of ZIF-67 and PMo$_{12}$ with different amount, which provides a platform for the construction of the bimetallic catalysts with different Co/Mo ratio. The scanning electron microscope (SEM), transmission electron microscopy (TEM) images and corresponding elemental mappings of ZIF-67 reveals the presence of uniform cubes with lateral size about 250 nm and smooth surface (Figs. 2b, c and S7). As displayed in Fig. 2d, after the addition of 0.125 g of PMo$_{12}$, the Co-Mo-0.125 precursor with a uniform nanocube morphology was successfully obtained, being similar to that of ZIF-67. The TEM images (Fig. 2e and f) show that the Co-Mo-0.125 precursor possesses an internal hollow structure, indicating that the ZIF-67 undergoes an etching reaction with the introduction of PMo$_{12}$. The scanning TEM (STEM) image and corresponding energy dispersive X-ray (EDX) mapping (Fig. 2g) show the homogeneous distribution of Co, Mo, C, N and O throughout the precursors.

To understand the evolution process of the hollow structure and to tune the ratio of Mo/Co, the amount of PMo$_{12}$ was changed in the synthesis. Figs. 3 and S8 show the evolution of the morphology. As displayed in Fig. 3a, in the case of adding low amount of PMo$_{12}$ (5 mg), the Co-Mo precursor (Co-Mo-0.005) still shows a solid cubic structure with a few nanosheets on the surface. Increasing the amount of PMo$_{12}$ to 50 mg could make the formation of the Co-Mo-0.050 precursor with still a solid structure (Fig. S8). It is worth noting that some void can be seen in the cubes. Further increasing the amount of PMo$_{12}$ to 60 mg (Fig. 3b) resulted in the formation of the Co-Mo-0.60 sample with many small holes in the interior. When the amount of PMo$_{12}$ was 70 mg, the internal pores gradually increased (Fig. 3c), and finally the hollow cubic structure was obtained with the further increase of PMo$_{12}$ amount to 110 mg (Fig. 3d).

Considering that PMo$_{12}$ tends to act as an anionic template/ structure-directing agent through host–guest supra-molecular interactions in the process of building PMo$_{12}$/ZIF-67 precursors [44,45], the PMo$_{12}$ can alter the equilibrium between the metal nodes and the organic ligands and regulate the morphology of the final products [46].
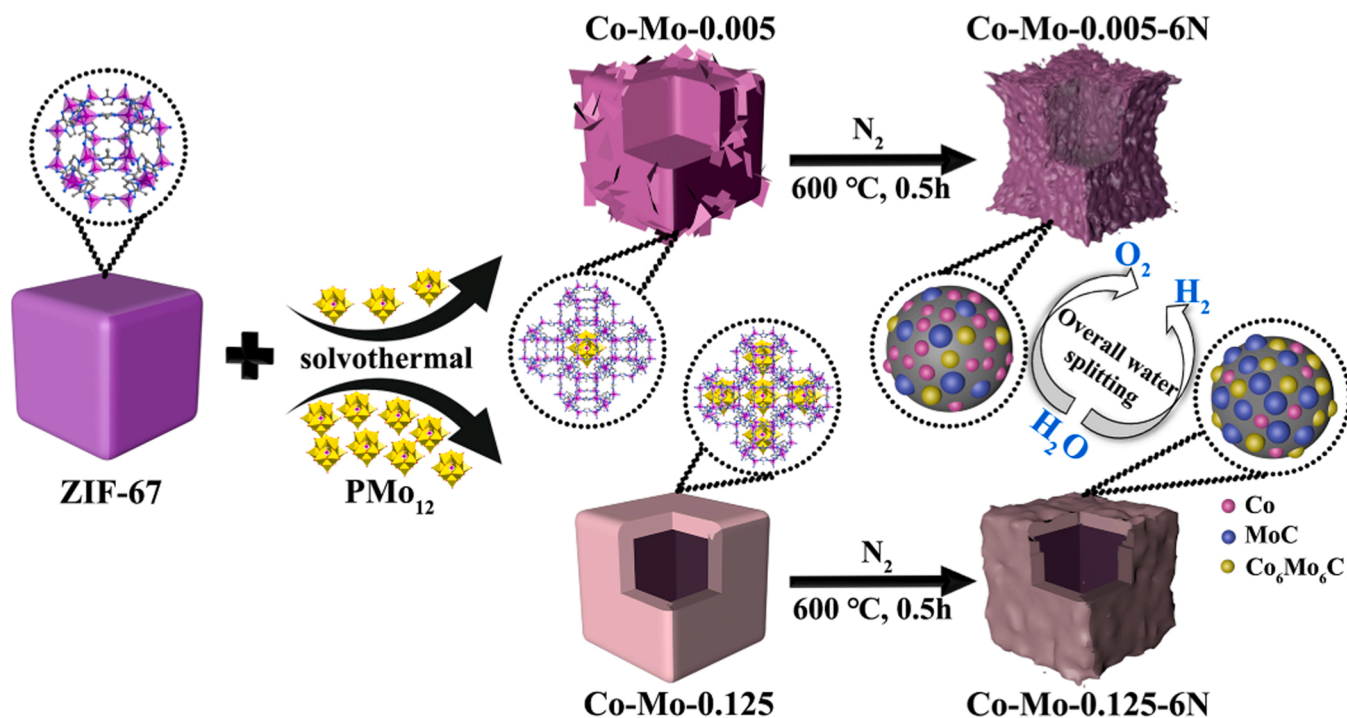
Fig. 1. Schematic illustration of the synthesis of uniform $Co_6Mo_6C/MoC/Co$ catalysts with tunable Co/Mo ratio and as coupled OER and HER catalysts for overall water splitting.

Hence, based on the above experiments and the relevant literatures, PMo_{12} will interact with Co ions in ZIF-67 during the reaction, which will destroy the original coordination between metal nodes and ligands, thus resulting in a dissolution and recrystallization process. In the case of low amount of PMo_{12}, the electrostatic interaction between PMo_{12} and Co ions is relatively weak. The reaction can only be carried out on the surface of ZIF-67, which makes the surface rough and a few nanosheets are formed, but still presents a solid structure. As the amount of PMo_{12} increases to an appropriate amount, the coordination between the metal nodes and organic ligands is inhibited by the PMo_{12}, resulting in the dissolution of ZIF-67 and the formation of porous structure. With the further increase of the amount of PMo_{12}, this influence of PMo_{12} occurs on more connecting nodes, which cause more serious damage to the interior of ZIF-67. The ions diffusion is unbalanced due to the fast outward diffusion of ions and slow inward diffusion, resulting in the formation of hollow structure [47,48]. The hollow structure can provide more active sites for electrochemical reactions. This synthesis strategy can regulate the ratio of Mo/Co and the micro-morphology, which is more conducive to improve the catalytic performance of the catalyst.

The bimetallic Mo-Co composites with adjustable Mo-Co ratio can be suitable precursor for the TMICs. Generally, the early TMICs can be suitable candidates for HER, but showing low OER activity. However, the later TMICs exhibits obvious OER activity. We proposed that a high Co/Mo ratio can give optimized OER activity, and high Mo/Co ratio is favourable to optimize HER activity. So, two typical Co-Mo based precursors, Co-Mo-0.005 with low Mo/Co ratio and Co-Mo-0.125 with high Mo/Co ratio were heat treated under N_2 atmosphere. The 2-MIM can provide carbon source for the conversion of the precursors into corresponding Co-Mo based carbides. Based on the ICP test, the content of Co in Co-Mo-0.005–6N is about 47.86%, and the content of Mo is about 8.37% (Table S2). The Co content in Co-Mo-0.125–6N is about 38.32%, and the Mo content is about 52.36% (Table S2). So, the Co-Mo based carbides with different Co/Mo ratio can be obtained by this route, which provides a platform for studying the effect of Co/Mo ratio on the HER/OER performance. From Fig. 4a, the diffraction peaks of Co_6Mo_6C (PDF# 80–0338), MoC (PDF# 89–2868) and Co phase (PDF# 89–7093)

can be observed, confirming the formation of $Co_6Mo_6C/MoC/Co$ composites. Fig. 4b shows the SEM image of the Co-Mo-0.005–6N sample. Compared with Co-Mo-0.005 precursor, the morphology of Co-Mo-0.005–6N sample changes greatly. The nanocubes shrink inward and nanoparticles are formed on the surface, which is mainly due to the decomposition of internal 2-MIM during heat treatment.

TEM image (Fig. 4c) shows that many small nanoparticles with sizes mainly below 10 nm are embedded in the polyhedron. Such a hierarchical structure with high surface roughness not only exposes abundant active sites but also avoids the aggregation of catalysts during the catalysis process, which is conducive to improving the catalytic performance. The high-resolution TEM image (Fig. 4d) shows the interplanar spacings of the lattice fringes of 0.20, 0.21 and 0.25 nm, corresponding to the (111) planes of metallic Co, (511) planes of Co_6Mo_6C and (111) planes of MoC, respectively. The energy-dispersive X-ray spectroscopy (EDX) elemental mapping images show that Co, Mo, C, N, and O are homogeneously distributed in Co-Mo-0.005–6N, while Co element is mainly located as the separated nanoparticles (Fig. 4e). Fig. 4f displays the XRD pattern of Co-Mo-0.125–6N. It can be seen that the diffraction peaks of Mo-containing components have high intensity, while the diffraction intensity of metal Co is relatively weak. This is because the Co-Mo-0.125 precursor contains more PMo_{12}, which reacts with more Co to form Co_6Mo_6C, and the remaining PMo_{12} is carbonized to form MoC. As known, there are N and C in the 2-methylimidazole of ZIF-67, which allows them to act as potential C source and N source for the formation of the nitrides and carbides. As shown in Fig. 4a and f, the diffraction peaks of Co_6Mo_6C, MoC and Co can be obviously seen. No peaks about the Co-Mo-N or Co-Mo-O can be observed in present XRD patterns. In addition, the previous reports have shown that the Mo-based carbides were usually formed by the pyrolysis of the precursor containing ZIF-67 and Mo components. So, it implied that the 2-methylimidazole is predominant C source to give carbides in present system, rather than nitrides and oxides [49–51]. Hence, the main components in Co-Mo-0.125–6N are Co_6Mo_6C, MoC and Co. Notably, when the content of PMo_{12} is less (Fig. 4a), the characteristic diffraction peaks intensity of Mo-containing products is weak and that of Co-containing products is
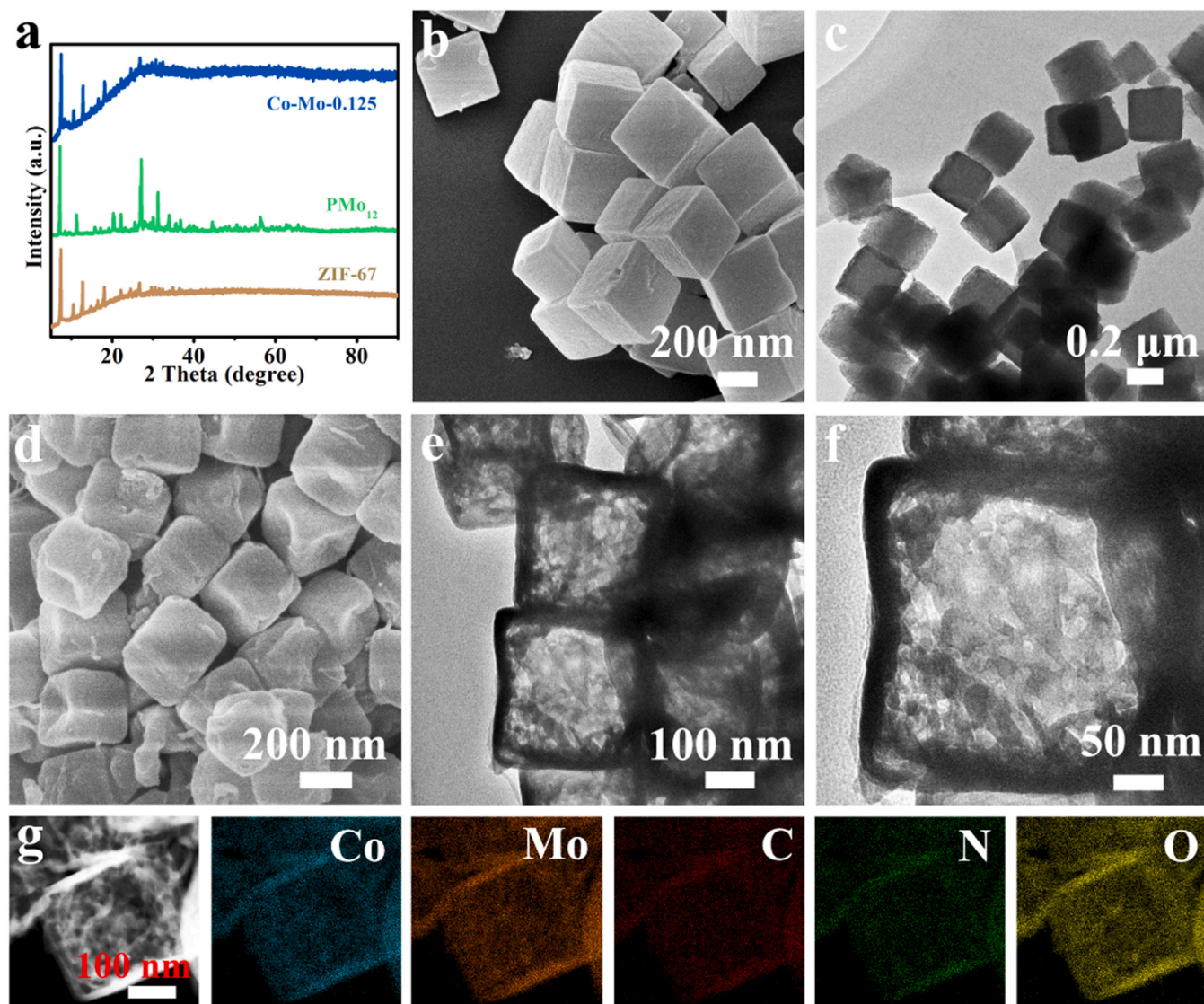
Fig. 2. (a) XRD patterns of Co-Mo-0.125, PMo$_{12}$ and ZIF-67; (b) SEM and (c) TEM images of ZIF-67; (d) SEM, (e-f) TEM images and (g) STEM image and EDX elemental mappings of Co-Mo-0.125 precursor.

strong, which is related to the low Mo/Co ratio. The analysis by XRD shows that the ratio of Mo/Co ratio in the precursor can adjust the proportion of Co-containing and Mo-containing components in the final Mo-Co based carbides. Fig. 4 g shows the SEM image of Co-Mo-0.125–6N. The Co-Mo-0.125–6N still maintains the cubic structure with a smooth surface, which may be due to Mo and Co being concentrated on the outside of the hollow Co-Mo-0.125 nanocube, resulting in a more stable structure. In addition, the slight adhesion between nanocubes is caused by the phase transformation in the pyrolysis process. The hollow nanocubic structure can be further observed by the TEM (Fig. 4 h). The presence of holes can facilitate the efficient diffusion of electrolyte and the exposure of more active sites. The HRTEM image (Fig. 4i) shows the lattice fringes of 0.21, 0.25 and 0.20 nm in the three adjacent areas, which are corresponding to the (511) plane of Co$_6$Mo$_6$C, (111) plane of MoC and (111) plane of Co, respectively. The STEM images and the corresponding elemental mappings reveal the uniform distribution of Mo, Co, C, N and O elements throughout the nanocubes (Fig. 4j). In addition, the EDX spectra of Co-Mo-0.005–6N and Co-Mo-0.125–6N also further indicate that the Mo/Co ratio in Co-Mo-based carbides is regulable (Fig. S9). The above analysis shows that by adjusting the content of the captured PMo$_{12}$, the morphology and the Co/Mo ratio in the product can be adjusted, thereby

adjusting the d electronic structure and the number of active sites to optimize HER and OER activity.

The formation of the heterojunctions can result in the re-distribution of the electrons at the interface, thus giving the active sites with enhanced activity. X-ray photoelectron spectroscopy (XPS) is used to study the surface electronics states of the typical samples. The XPS survey spectra show the presence of Co, Mo, C, N, O and P in Co-Mo-0.005–6N and Co-Mo-0.125–6N (Fig. 5a). Fig. 5b presents the Co 2p XPS spectra of the Co-Mo-0.005–6N and Co-Mo-0.125–6N samples. The four components of Co^0, Co^{2+}, Co^{3+} and satellite peaks (identified as "Sat.") constitute the Co 2p core energy level spectrum. In the deconvoluted Co 2p XPS spectrum of Co-Mo-0.005–6N, the peaks situated at 797.80 and 782.00 eV are attributed to Co^{2+} in Co$_6$Mo$_6$C, accompanied by two satellite peaks at 785.90 and 802.79 eV [52]. Two peaks at 780.11 eV and 795.87 eV are attributed to the oxidation-state of Co^{3+} from slight surface oxidation [41]. The peaks at 778.30 and 793.80 eV in the high-resolution spectrum of Co 2p can be assigned to the Co metal (Co^0), which is consistent with the XRD results [53,54]. The high-resolution XPS of the Mo 3d region of Co-Mo-0.005–6N (Fig. 5c) shows two peaks at 229.35 and 232.85 eV belonging to Mo^{2+} of the Mo-C bond in Co$_6$Mo$_6$C and MoC [55]. The peaks at 232.15 eV and 235.30 eV belong to Mo^{6+}, which is from probably oxidation of carbide [56].
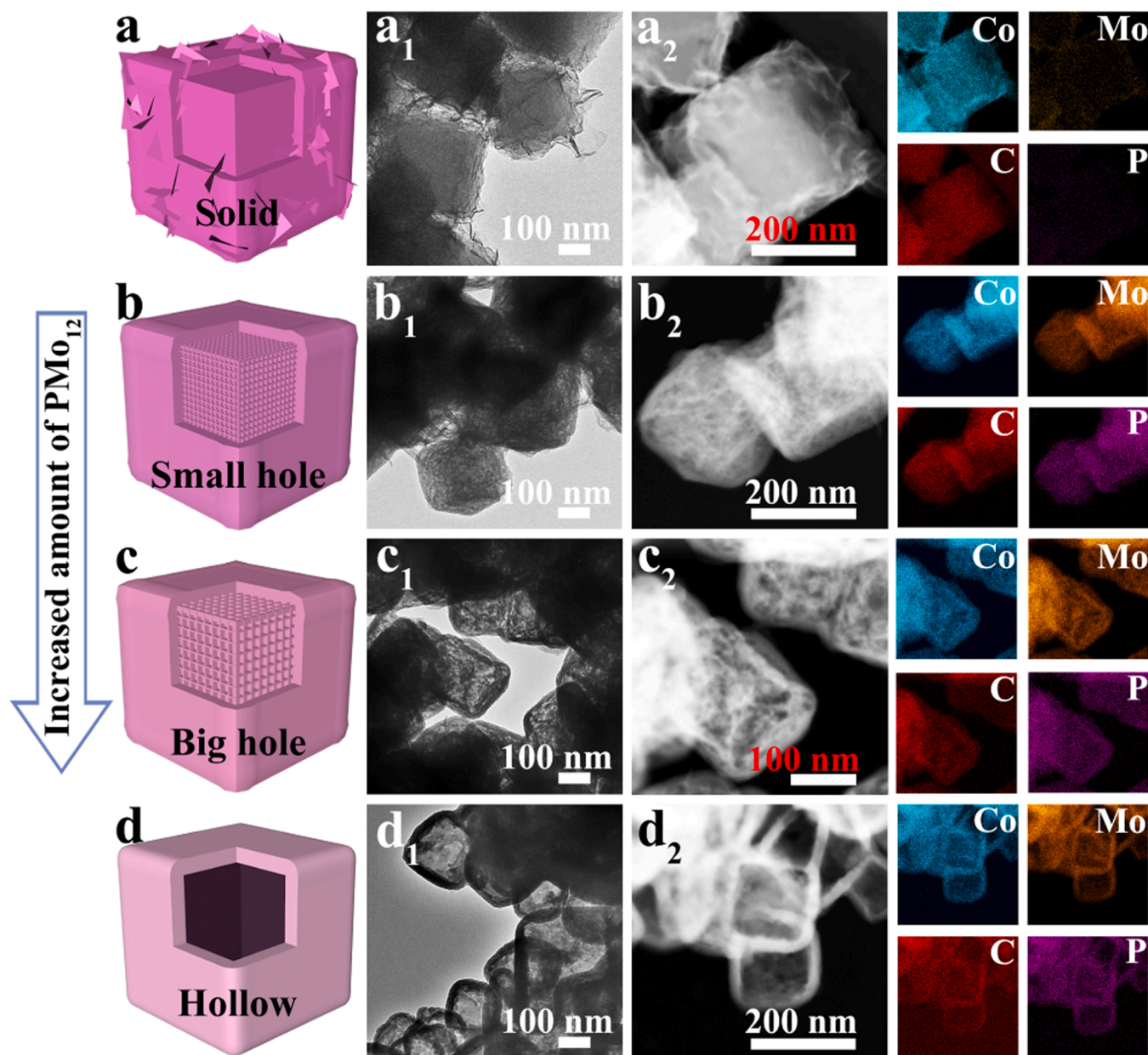
Fig. 3. Schematic presentation of the morphology evolution process of hollow nanocubes, and the corresponding TEM, STEM images and corresponding EDS elemental mapping for the samples obtained at different amounts of PMo_{12}: (a) 5 mg, (b) 60 mg, (c) 70 mg and (d) 110 mg.

Although Co-Mo-0.125–6N and Co-Mo-0.005–6N have the same components, the main elements in the two samples show different bonding energy, which implies the difference in the interfacial electron redistribution. For Co-Mo-0.125–6N, the peaks at 781.60/797.40 eV, 780.04/795.80 eV, 778.12/793.62 eV and 785.78/802.67 eV can be attributed to the Co^{2+}, Co^{3+}, Co^0 and satellite peaks, respectively. Compared with the Co 2p XPS spectrum of Co-Mo-0.005–6N, the Co^{2+} peaks in Co-Mo-0.125–6N have a negative shift of 0.3 eV (Figure 5b$_1$). In addition, the Co^0 2p peaks in Co-Mo-0.005/0.125–6N have a positive shift compared with the Co sample [57]. Fig. 5c shows the Mo XPS spectrum of the Co-Mo-0.125–6N samples. Two doublets at 230.00/233.50 eV and 232.10/235.25 eV are assigned to the Mo 3d$_{5/2}$ and Mo 3d$_{3/2}$ of the Mo^{2+} and Mo^{6+}, respectively. It is clearly seen that the Mo^{2+} peaks in Co-Mo-0.125–6N have a positive shift of 0.65 eV compared with that of the Co-Mo-0.005–6N sample (Figure 5c$_1$). Compared with the Mo^{2+} 3d XPS spectrum of MoC, the Mo^{2+} 3d peaks for Co-Mo-0.005/0.125–6N shift positively [58]. The above results

indicate that electron transfer occurs between the Co and Mo components, which can tune the interfacial electronic structure and improve the catalytic performance. Remarkably, the difference in the interfacial electron redistribution can result in the different catalytic ability. The C 1 s spectrum of Co-Mo-0.005–6N and Co-Mo-0.125–6N (Fig. 5d) shows five sub-units at approximately binding energies of 284.60, 285.18, 284.41, 286.46 and 288.46 eV, ascribing to the C-M (Metal), C-N, C-C/C=C, C-O and C=O [41]. In addition, the high-resolution N 1 s peaks can be divided into two peaks, indexing to pyridinic-N and pyrrolic-N and the two peaks in high-resolution P 2p spectra can be ascribed to the P-O and P-C (Fig. S10) [41]. The existence of N and P doped carbon are mainly due to the pyrolysis of 2-MIM and PMo_{12}, which can contribute to the electrocatalytic activity.

A series of control experiments show that the experimental parameters can affect the component and micro-structure of the final catalysts. As shown in Figs. S11-S12, when raw ZIF-67 (without the addition of Mo) was calcined under the same conditions, only Co_3C (Co-6N) can be
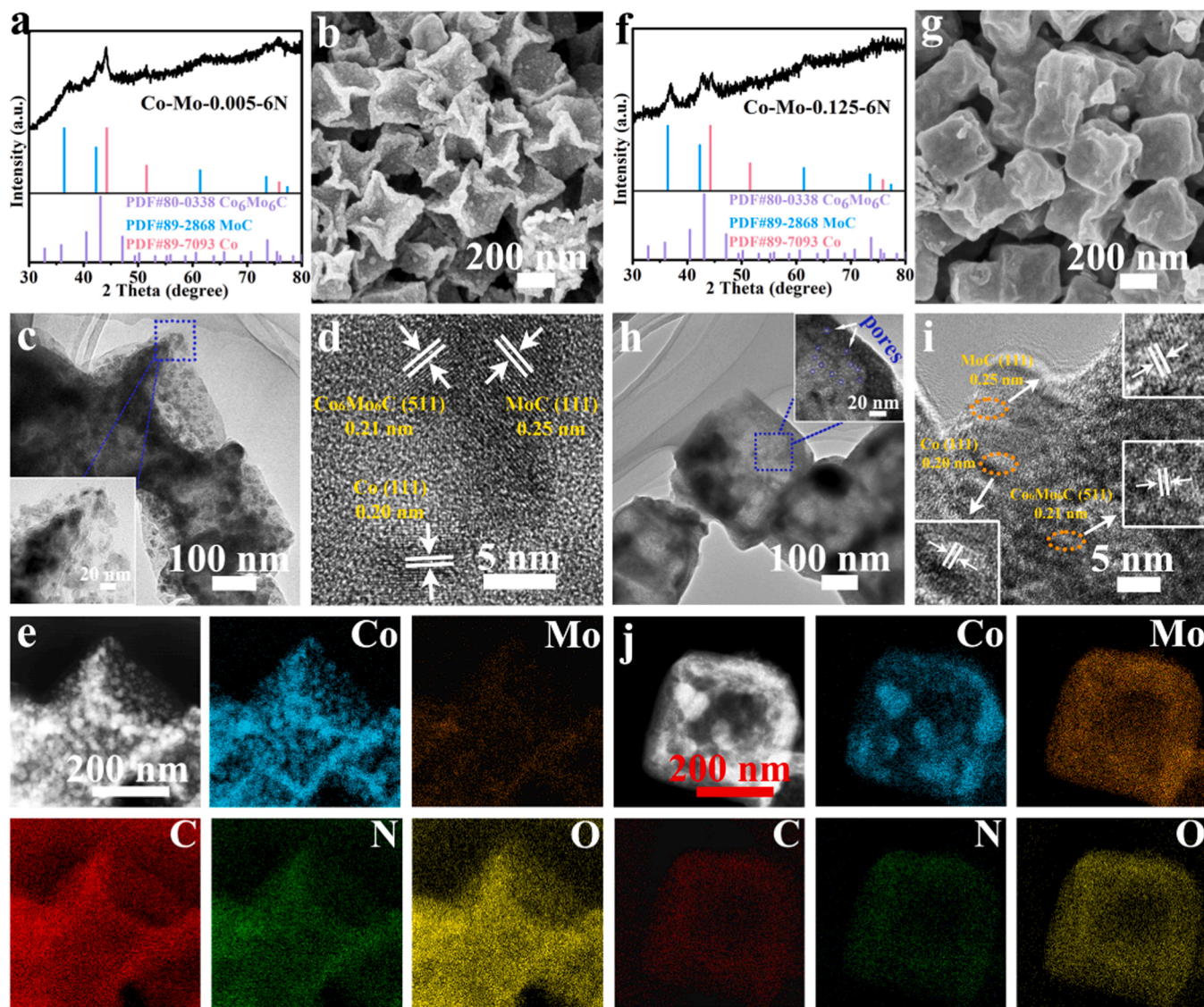
Fig. 4. (a, f) XRD patterns, (b, g) SEM, (c, h) TEM, (d, i) HRTEM images, (e, j) STEM images and the corresponding elemental mapping of Co, Mo, C, N and O of Co-Mo-0.005–6N (a-e) and Co-Mo-0.125–6N (f-j) electrocatalyst.

formed. The SEM and TEM images (Fig. S13) of Co-6N show that the nanocube was greatly destroyed and numerous nanoparticles were generated. This indicates that the introduction of PMo_{12} can enhance the morphological stability of the materials during the pyrolysis. The pyrolysis temperature also has a great influence on composition and microstructure. Figs. S14-S21 show that at low calcination temperatures, the crystallinity of the product is poor, which is mainly caused by incomplete carbonization at low temperature, while the higher temperature endows the higher carbon thermal reduction capacity, which is conducive to the formation of BTMCs with higher crystallinity. In addition, the morphologies of the obtained samples are well maintained, proving the good structural stability.

3.2. Electrocatalytic hydrogen evolution performance and mechanism analysis

The HER performance of the as-prepared catalysts was first evaluated in 1 M KOH by adopting a standard three-electrode system, in which the carbon rod and Hg/HgO electrode were used as counter electrode and reference electrode, respectively. The polarization curves were obtained by linear sweep voltammetry (LSV) test without iR-

correction. As displayed in Figs. 6a and S22a, the Co-Mo-0.125–6N catalyst shows the best HER activity among all as-prepared samples with a nearly zero onset potential. As shown in Figs. 6b and S22b, the Co-Mo-0.125–6N only needs an overpotential of 52 mV to achieve a current density of 10 mA cm^{-2}, which is much lower than those of Co-Mo-0.005–6N (67 mV), Co-Mo-0.025–6N (70 mV), Co-Mo-0.05–6N (75 mV), Co-Mo-0.1–6N (79 mV). On the contrary, the sample obtained without the introduction of Mo source (Co-6N) requires large overpotential of 106 mV to attain 10 mA cm^{-2}. This result demonstrates that the introduction of Mo source to construct $Co_6Mo_6C/MoC/Co$ multicomponent heterojunction can effectively improve the catalytic performance of the material. Notably, the catalyst with high Mo/Co ratio is more suitable for the HER, which may be because the high Mo/Co ratio leads to the increase of Co_6Mo_6C and MoC content in $Co_6Mo_6C/MoC/Co$ heterojunction. MoC is considered as an ideal HER material due to its electronic structure similar to that of precious metals [59–61]. Moreover, Co_6Mo_6C can dramatically enhance the HER catalytic activity because the interaction between two metals can modulate the local electronic density and enrich active sites [62].

In order to eliminate the influence of Ohmic resistance, the LSV data with 90% iR compensation of the Co-Mo-X-6N and Co-6N catalysts were
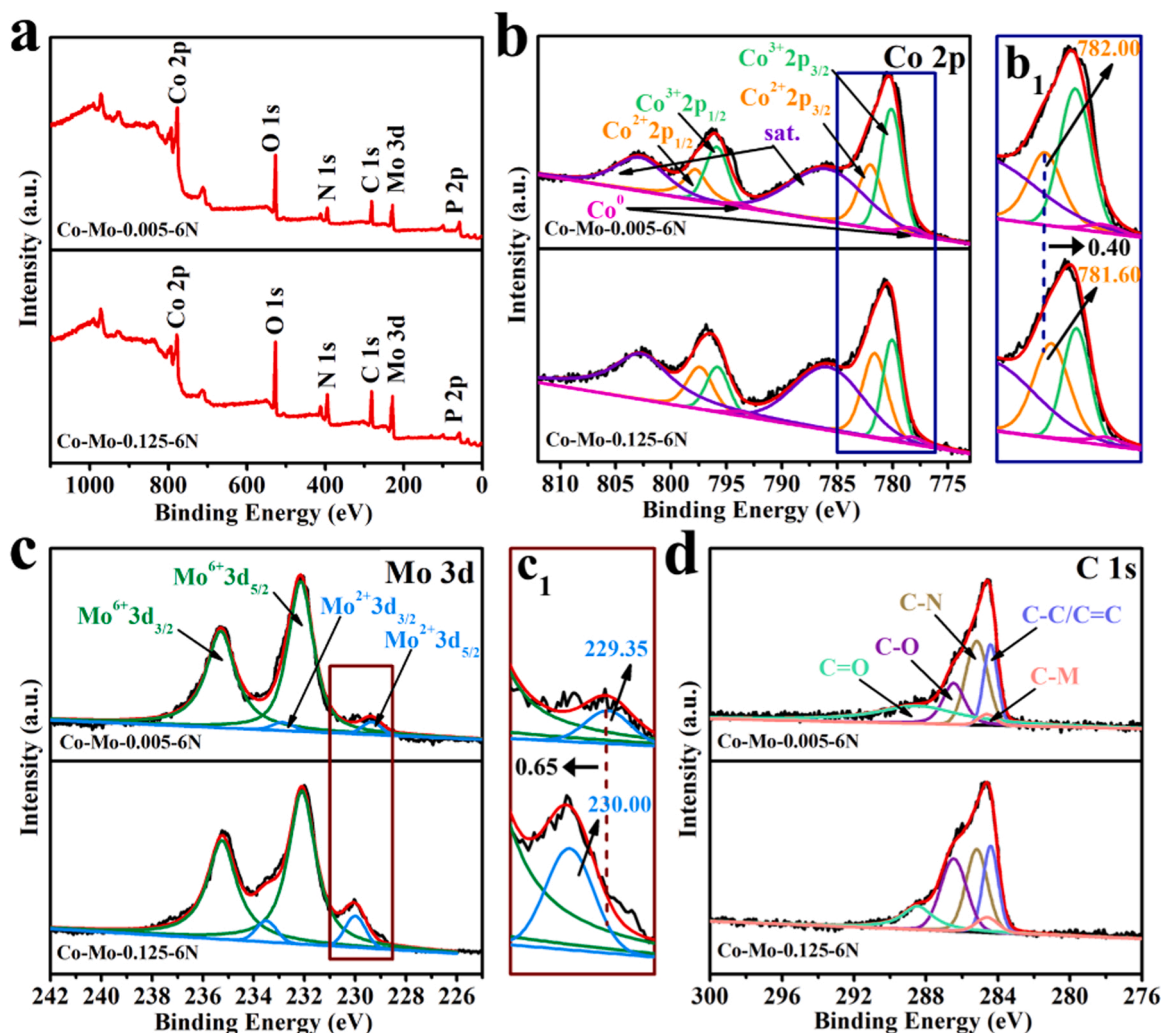
Fig. 5. (a) XPS survey spectra and the high-resolution XPS spectra of (b) Co 2p, (c) Mo 3d and (d) C 1 s for Co-Mo-0.005–6N and Co-Mo-0.125–6N.

also provided. As shown in Fig. S23, all Co-Mo-*X*-6N samples only need a low overpotential to deliver a high current density. For Co-Mo-0.125–6N catalyst, the required overpotentials are only 30 and 77 mV at the current density of 10 and 100 mA cm^{-2}, respectively, showing excellent HER performance at large current density. Tafel slope is an essential parameter to study the HER kinetics. As presented in Fig. 6c, the Tafel slope for Co-Mo-0.125–6N is 54 mV dec^{-1}, much smaller than those of Co-6N (96 mV dec^{-1}), Co-Mo-0.005–6N (66 mV dec^{-1}) and Co-Mo-0.05–6N (82 mV dec^{-1}), suggesting that Co-Mo-0.125–6N sample exhibits the most favorable kinetics for the HER via the Volmer-Heyrovsky mechanism. The catalytic activity is related to the number of active sites. The electrochemical specific surface area (ECSA) is usually calculated to evaluate the number of active sites, and it is proportional to the double layer capacitance (C$_{dl}$), which was measured by Cyclic voltammetry (CV) in the voltage range of 0.10–0.20 V (vs. RHE) with different scan rates (Figs. S24-S25). As shown in Figs. 6d and S25c, the C$_{dl}$ value of Co-Mo-0.125–6N is 85.5 mF cm^{-2}, being higher than those of Co-6N (8.5 mF cm^{-2}), Co-Mo-0.005–6N (76.5 mF cm^{-2}), and Co-Mo-0.05–6N (66.5 mF cm^{-2}) and other control samples. When current density was normalized for ECSA (Fig. S26), the Co-Mo-0.125–6N still shows better HER performance than the other catalysts, implying a higher intrinsic catalytic activity of Co-Mo-0.125–6N. As shown in Fig. S27, the Co-Mo-0.125–6N catalyst has the highest turnover frequency (TOF) of 0.433 s^{-1} at the potential of − 0.1 V, which is higher than those of Co-6N (0.018 s^{-1}), Co-Mo-0.005–6N (0.279 s^{-1}), Co-Mo-0.025–6N (0.212 s^{-1}), Co-Mo-0.05–6N (0.073 s^{-1}), Co-Mo-0.1–6N (0.037 s^{-1}),

indicating a high instantaneous efficiency for HER catalysis. Furthermore, the electrochemical impedance spectroscopy spectra (Fig. 6e) reveal the fast HER kinetics of Co-Mo-0.125–6N toward the interface between catalyst and electrolyte. The low charge transfer resistance of Co-Mo-0.125–6N should be due to strong synergistic effect between Co$_6$Mo$_6$C, MoC and Co that can significantly increase the electron transfer rate. Besides good activity, the Co-Mo-0.125–6N also displays good stability for HER. As shown in Fig. 6f, the polarization curve of Co-Mo-0.125–6N catalyst after 3000 consecutive CV cycles almost overlaps with the original one. Furthermore, the i-t curve shows that the current density remains almost unchanged for 48 h, further demonstrating its excellent catalytic stability for HER in 1 M KOH (Fig. 6f illustration). In addition, the SEM image, XRD pattern and XPS spectrum of Co-Mo-0.125–6N after the HER test showed that the Co-Mo-0.125–6N catalyst had good structural and compositional stability for HER (Fig. S28). As noted above, Co-Mo-0.125–6N exhibits remarkable activity and excellent durability. The HER performance of Co-Mo-0.125–6N surpasses most of the reported double transition metal based electrocatalysts in alkaline electrolyte (Fig. 6g and Table S3).

The remarkable HER performance can be attributed to the following reasons. Primarily, hollow nanostructures could provide more active sites for electrochemical reactions. Besides, rational regulation of the proportion of Co-containing and Mo-containing components and heterojunction engineering can tune the electronic structure of the catalyst, thus improving the catalytic performance. Rational tuning of the Co/Mo ratio could decrease the empty d-orbital density and valence states of
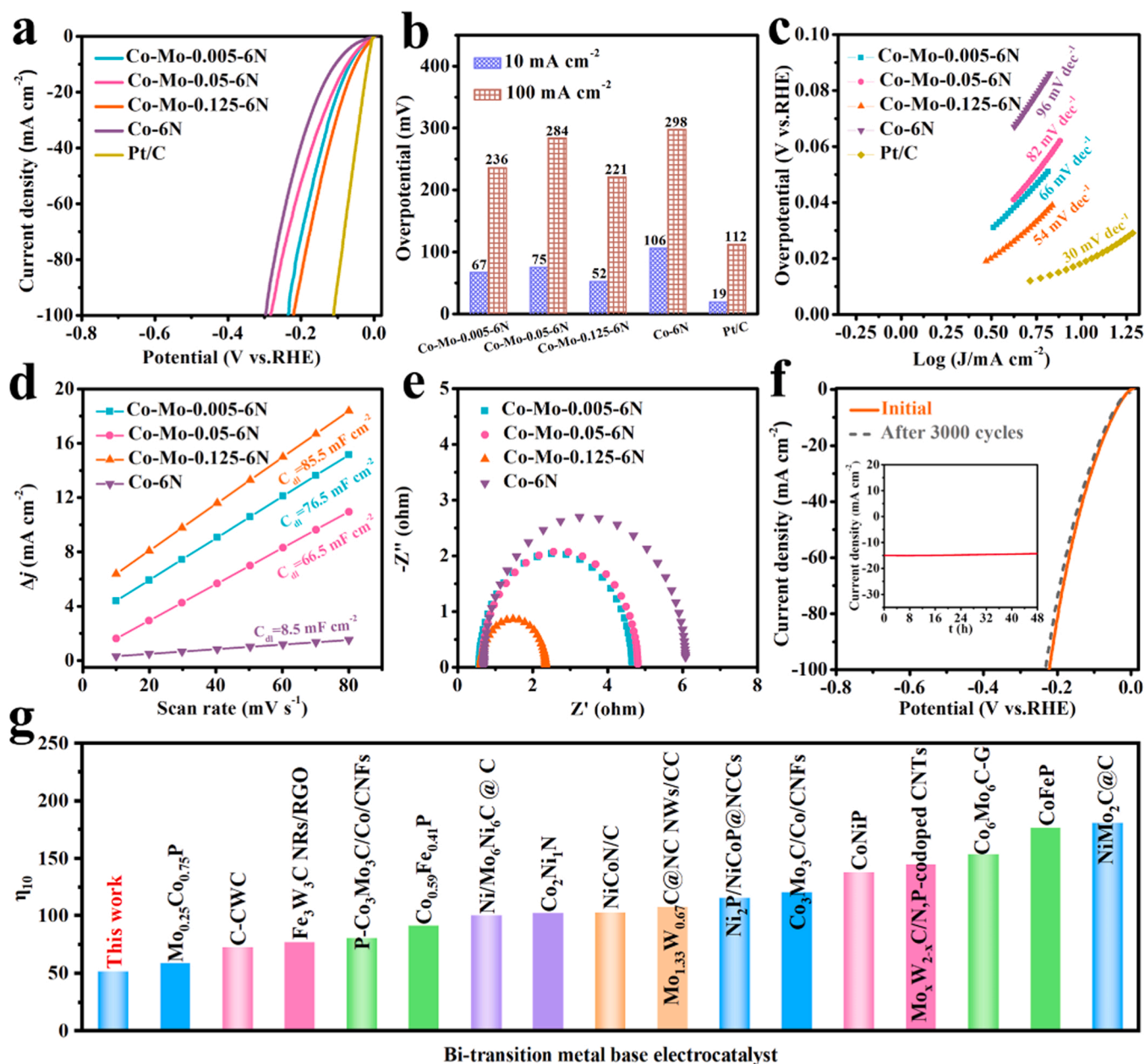
Fig. 6. (a) Polarization curves, (b) related overpotential, and (c) corresponding Tafel plots of Co-Mo-0.005–6N, Co-Mo-0.05–6N, Co-Mo-0.125–6N, Co-6N and Pt/C in 1 M KOH; (d) Plots showing extraction of the double-layer capacitance (C_{dl}) and (e) corresponding Nyquist plots of different electrode for HER; (f) Polarization curves for Co-Mo-0.125–6N electrocatalyst before and after 3000 cycles of CV test. Inset: the current-time (I-t) curves of Co-Mo-0.125–6N electrocatalyst for 48 h; (g) Comparison of η_{10} for HER with reported bi-transition metal base electrocatalyst.

Mo, which is an efficient way to optimize the HER performance [63]. To gain further insights into the HER catalytic performance of Co-Mo based catalysts with different Co/Mo ratio, density functional theory (DFT) calculations were performed. Based on the structural characterization and experimental results, three simplified models with different Co/Mo ratio (Co-MoC model consisting of metallic Co cluster on MoC, MoC-Co model consisting of MoC cluster on metallic Co and Co-MoC composite model) were built, shown in Fig. 7a. The charge density differences (Figs. 7b and S29) illustrate that there is electron accumulation at the interface, suggesting a strong charge interaction between Co and MoC.

The hydrogen adsorption Gibbs free energy (ΔG_{H*}) is an appropriate parameter for evaluating the HER activity. For an optimal catalyst, the $|\Delta G_{H*}|$ should be awfully close to zero from the viewpoint of thermodynamics, which makes both H* desorption and adsorption more easily. The adsorption energies of H* on the surfaces of the (111) facet of

metallic Co, the (111) facet of pristine MoC, the (100) facet of Co_6Mo_6C and different Co (Mo) sites in Co-MoC, Co-MoC composite and MoC-Co were calculated (Figs. 7c and S30-S36). As shown in Fig. 7c, the H* adsorption on metallic Co (0.72 eV) and Co_6Mo_6C (0.76 eV) were too strong, suggesting H* was difficult to desorb, leading to a low catalytic activity toward HER. Notably, after constructing the Co/MoC interfaces, the $|\Delta G_{H*}|$ value decreased obviously, indicating the synergistic interaction of Co and MoC has a positive effect on enhancing the HER performance. The $|\Delta G_{H*}|$ value on the Co site 1 in Co-MoC was calculated to be 0.21 eV, which is smaller than those on Mo site 1 in Co-MoC (0.30 eV), Co site 2 in MoC-Co (0.32 eV), Mo site 2 in MoC-Co (0.69 eV), Co site in Co-MoC composite (0.78 eV) and Mo site in Co-MoC composite (0.61 eV), from which it can be inferred that Co sites are more favorable for H adsorption and desorption during the Heyrovsky step. Clearly, the combination of Co cluster and MoC adjusts the
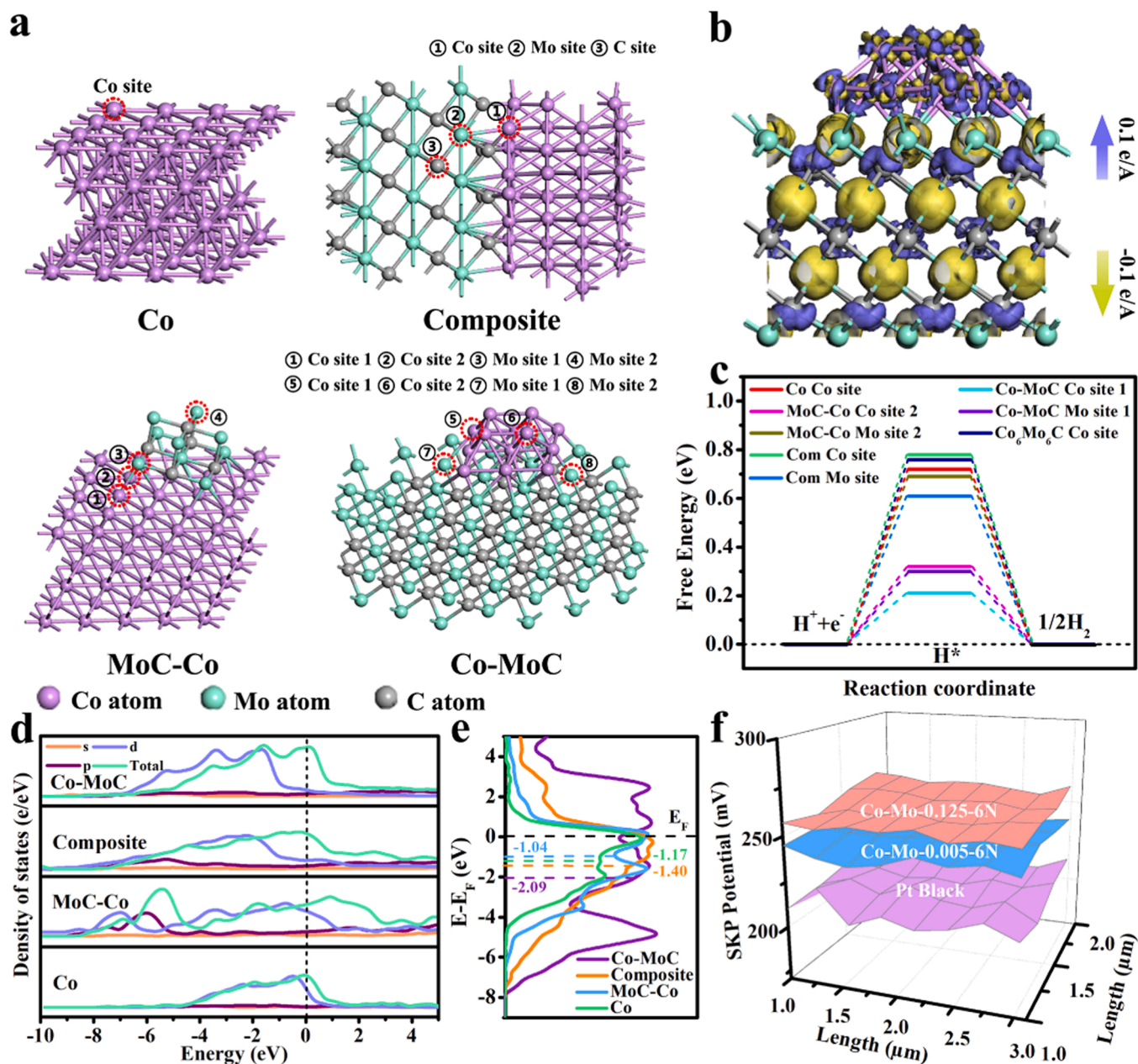
Fig. 7. (a) Geometricmodel of Co, MoC-Co, Co-MoC composite and Co-MoC; (b) Electron density plot at the Co-MoC; (c) Free-energy diagram of ΔG_{H*}; (d) DOS of Co, MoC-Co, Co-MoC Composite and Co-MoC system; (e) Calculated partial density of state (DOS) of Co, MoC-Co, Co-MoC Composite and Co-MoC system; (f) Work function (WF) drawings of Pt/C, Co-Mo-0.005–6N, Co-Mo-0.125–6N.

electronic structure, resulting in lower $|\Delta G_{H*}|$ value on Co site 1 compared with that on the Co-MoC composite and MoC-Co, which suggests that low ratio of Co/Mo in $Co_6Mo_6C/MoC/Co$ catalysts is more favorable for optimizing the H adsorption and desorption during the HER, which is consistent with the electrochemical measurement results. It is well known that the HER process in alkaline electrolyte is generally depicted as three-state, including the initial catalyst-H_2O state, the intermediate catalyst-H* state, and the final catalyst-H_2 state. Therefore, the adsorption energy of H_2O on the surfaces of different catalysts were also calculated (Figs. S37-S39). As shown in Fig. S40, the Co-MoC catalyst possesses a lower water adsorption energy (−12.03 eV) than that of Co (−1.46 eV), MoC (−3.58 eV), Co_6Mo_6C (−3.12 eV), MoC-Co (0.87 eV) and Co-MoC composite (−7.60 eV), suggesting the initial catalyst-H_2O state can easily occur on the surface of Co-MoC catalyst to facilitate the HER process. Moreover, the continuous distribution of the density of states (DOS) near the Fermi level, as shown in Fig. 7d,

indicates that Co-Mo based carbides are in a metallic state, which is beneficial for achieving high electronic conductivity. To gain insight into the effect of d-electron modulation on HER performance, the partial densities of states (DOS) of Co, MoC-Co, Co-MoC composites, and Co-MoC systems were calculated. The DFT calculation results show that the d-band center (ε_d) of Co-MoC with high Mo/Co ratio moves downward to − 2.09 eV, which is lower than those of Co (−1.17 eV), MoC-Co (−1.04 eV), Co-MoC composite (−1.40 eV) (Fig. 7e). The lower ε_d induced weaker adsorption and easier desorption of H on catalytic surface, thus optimizing the Gibbs free energy of hydrogen adsorption to promote intrinsic electrocatalytic activity. In addition, a good catalyst for HER should capture more electrons to promote the subsequent HER reaction. Work function (WF) is one of the most fundamental surface properties of a material, which can affect the reaction rate of HER. The WF of Pt/C, Co-Mo-0.005–6N, Co-Mo-0.05–6N, Co-Mo-0.125–6N and Co-6N are 5.63, 5.58, 5.56, 5.60 and 5.53 eV, respectively, calculated
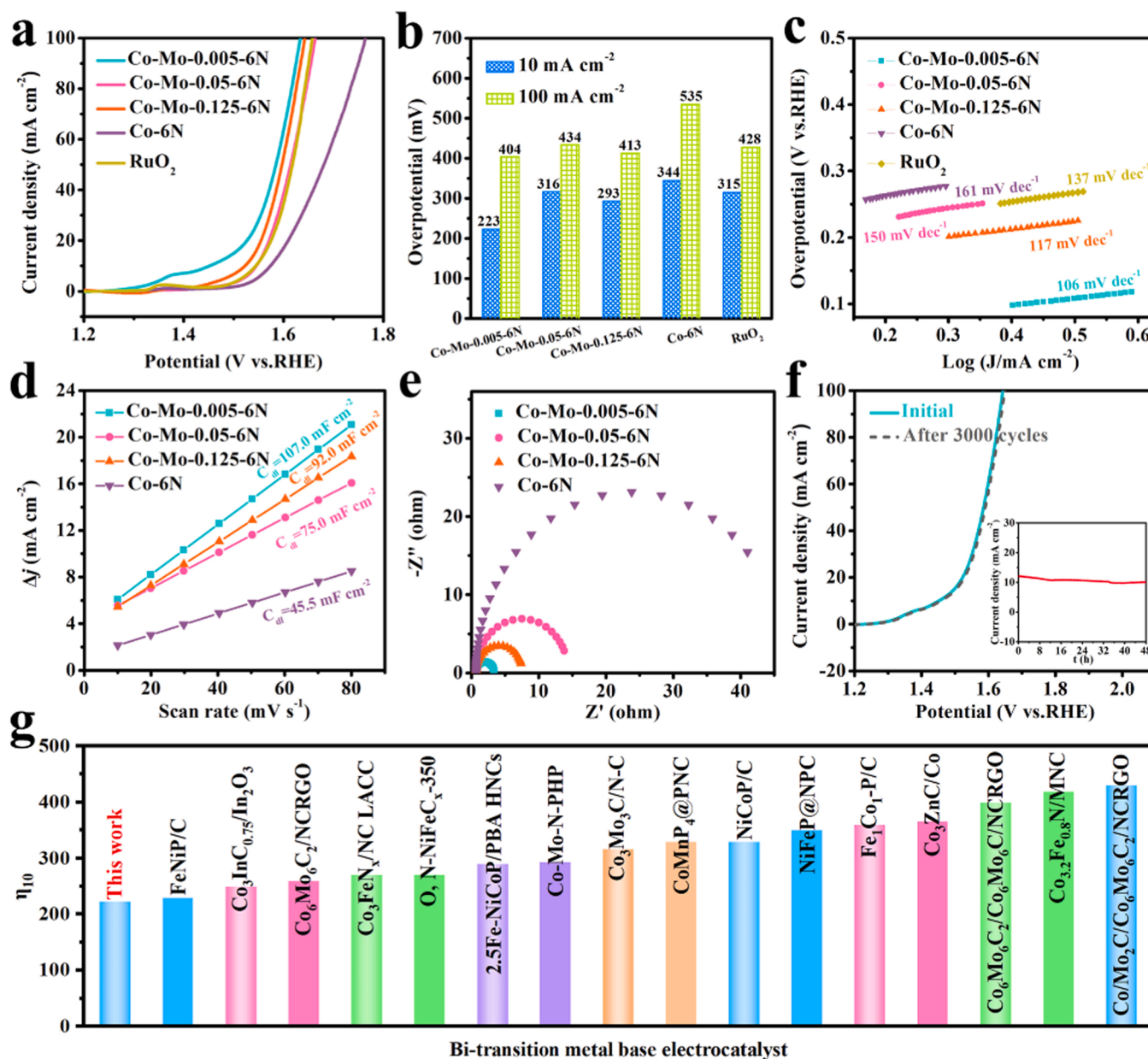
Fig. 8. (a) Polarization curves, (b) related overpotential, and (c) corresponding Tafel plots of Co-Mo-0.005–6N, Co-Mo-0.05–6N, Co-Mo-0.125–6N, Co-6N and Pt/C in 1 M KOH; (d) Plots showing extraction of the double-layer capacitance (C_{dl}) and (e) corresponding Nyquist plots of different electrode for OER; (f) Polarization curves for Co-Mo-0.005–6N electrocatalyst before and after 3000 cycles of CV test. Inset: the current-time (I-t) curves of Co-Mo-0.005–6N electrocatalyst for 48 h; (g) Comparison of η_{10} for OER with reported bi-transition metal base electrocatalyst.

based on scanning Kelvin probe (SKP) test (Figs. 7f and S41). The work function value of Co-Mo-0.125–6N is higher than that of other samples and close to Pt/C, indicating a stronger electron enrichment ability, which makes the easy reduction of H* to H_2 on Co-Mo-0.125–6N, thus giving enhanced HER activity.

3.3. Electrocatalytic oxygen evolution performance

The BTMCs materials have a good application prospect in catalytic OER, and the effect of each component in $Co_6Mo_6C/MoC/Co$ for OER was investigated. As shown in Figs. 8a-b and S22c-22d, different from the HER performance trend, the Co-Mo-0.005–6N catalyst with low Mo/ Co ratio shows the best OER activity with a low overpotential of 223 mV at 10 mA cm^{-2}, which is smaller than those of Co-6N (344 mV), RuO_2 (315 mV), Co-Mo-0.025–6N (239 mV), Co-Mo-0.05–6N (316 mV), Co-Mo-0.1–6N (317 mV) and Co-Mo-0.125–6N (293 mV), suggesting the

contribution of different components to OER activity is different. Moreover, after 90% iR compensation, the Co-Mo-0.005–6N catalyst only requires low overpotentials of 165 and 357 mV to achieve the current density of 10 and 100 mA cm^{-2}, respectively (Fig. S42). Moreover, in order to exclude the effect of oxidation peak, the reversal LSV scan test was performed for Co-Mo-0.005–6N (Fig. S43). The calculated overpotential (η_{10} of 240 mV) from the backward polarization curve is also very low, further demonstrating the significant activity of Co-Mo-0.005–6N for OER. The high OER activity of Co-Mo-0.005–6N should be ascribed to the higher content of Co and Co_6Mo_6C in the sample. Particularly, according to previous research, Co-containing components can not only enhance the electrical conductivity of catalyst, but also act as the pre-catalysts for the formation of OER active sites [64,65]. Therefore, $Co_6Mo_6C/MoC/Co$ heterostructures with high content of Co and Co_6Mo_6C are beneficial for increasing active sites and boosting the sluggish kinetics. Fig. 8c shows the Tafel slope of all catalysts for OER.

The Tafel slope of Co-Mo-0.005–6N catalyst is 106 mV dec^{-1}, which is lower than those of Co-6N (161 mV dec^{-1}), Co-Mo-0.05–6N (150 mV dec^{-1}), Co-Mo-0.125–6N (117 mV dec^{-1}), demonstrating the more favorable reaction kinetics of the Co-Mo-0.005–6N for water oxidation. As displayed in Fig. 8d, the C_{dl} value of Co-Mo-0.005–6N, Co-6N, Co-Mo-0.05–6N, and Co-Mo-0.125–6N are 107.0, 45.5, 75.0 and 92.0 mF cm^{-2}, respectively. Obviously, the Co-Mo-0.005–6N has the largest C_{dl} value among all comparative samples (Figs. 8d and S44-S45). The larger C_{dl} values and higher current density of the ECSA-normalized LSV (Fig. S46) indicates that the Co-Mo-0.005–6N catalyst has obvious advantages over other catalysts in terms of active surface area and active sites. Additionally, the small semicircle in electrochemical impedance spectroscopy (EIS) for Co-Mo-0.005–6N confirms its fast charge transfer efficiency, corresponding well with the higher conductivity of Co and metal carbides (Fig. 8e). Further, apart from high catalytic activity, Co-Mo-0.005–6N also exhibits good stability for OER in 1 M KOH. Typically, the well-over-lapped LSV curves before and after CV tests and the well-maintained current density at a set potential after the 48 h OER test confirm the remarkable electrocatalytic durability of Co-Mo-0.005–6N catalyst during the OER process (Fig. 8 f). As shown in Fig. 8 g and Table S4, the performance of Co-Mo-0.005–6N is also superior to most reported bi-transition metal based OER catalysts.

According to the research literature, P-doped is effective for turning the electronic structure, reducing the kinetic energy barrier, and introducing additional active sites [66–68]. The existence of a small amount of P in PMo$_{12}$ can result in the presence of P in the final catalysts, thus promoting the catalytic performance. To demonstrate the positive role of P, molybdenum sources without P in the structure (H$_4$SiMo$_{12}$O$_{40}$) were used in the synthesis for comparative experiment. As shown in Fig. S47, the performance of the typical HER catalyst (Co-Mo-0.125–6N) obtained by using phosphomolybdic acid as Mo source is better than that of the catalysts obtained by using other Mo sources (Co-SiMo$_{12}$–0.125–6N, η_{10} of 115 mV), indicating that P-doped improves the HER performance [69,70]. Moreover, Fig. S48 showed that Co-Mo-0.005–6N has a lower overpotential than that of Co-SiMo12–0.005–6N (η_{10} of 228 mV), which indicated that P doping has a positive effect on the OER process [71,72]. Therefore, we believe that the existence of a small amount of P in PMo$_{12}$ is conducive to the improvement of catalytic performance. Moreover, in order to explore the influence of metal Co on electrochemical performance, the obtained Co-Mo-0.005–6N and Co-Mo-0.125–6N sample were dispersed in 1.0 M HCl for 6 h to remove the Co nanoparticles and the corresponding products are named Co-Mo-0.005–6N-E and Co-Mo-0.125–6N-E, respectively (Fig. S49). After etching Co nanoparticles, the HER performance of Co-Mo-0.125–6N-E did not change significantly, while the OER performance of Co-Mo-0.005–6N-E decreased significantly, which suggested that the catalytic active components for HER and OER are different (Figs. S50-S51). After the etching of Co, the HER performance of the catalyst has only a little change. However, this does not mean that Co is not active component for HER based on the following analyses. First, as shown in previous study, the Co particles can not be completely removed in dilute HCl, making the possible residual of Co clusters [73]; 2) DFT calculation shows that the HER activity of Co-MoC is significantly better than that of MoC and Co$_6$Mo$_6$C, indicating that the formation of heterojunction with a small amount of Co is beneficial to improve the HER performance. For OER, the Co-O species formed in the original OER test are considered to be the catalytic active ingredients [74]. The difference in components of Co-Mo-0.005–6N and Co-Mo-0.125–6N (the different Co/Mo ratio) will affect the formation of the oxygen-containing species, thus resulting in different catalytic ability. In Co$_6$Mo$_6$C/MoC/Co catalyst, the metal Co is easily oxidized in KOH to form Co-O species under the OER test. The XRD pattern and XPS spectrum of Co-Mo-0.005–6N after 40 CV cycles of OER testing show the presence of Co(OH)$_2$ and the decrease of the content of metal cobalt, indicating the oxidation of metal Co in Co-Mo-0.005–6N (Figs. S52-S54). Co(OH)$_2$ will be further oxidized to form CoO$_x$ species in the OER

process which are the active species of the OER [75,76]. Therefore, higher Co/Mo ratio in the Co$_6$Mo$_6$C/MoC/Co catalyst will lead to better OER catalytic activity. In addition, the generated MoO$_x$ species (Fig. S54) will further promote OER performance [77]. Furthermore, the SEM image of Co-Mo-0.005–6N after OER (Fig. S55) further indicates the surface reconstruction during the OER. The phenomenon was frequently observed for the OER catalysts. Hence, the enhancement of OER activity of Co-Mo-0.005–6N should be attributed to the synergistic effect of the three phases of Co, MoC and Co$_6$Mo$_6$C on the formation of active species under the OER test. Moreover, we found that the calcination temperature has a large effect on the structure and composition of the catalysts, thus affecting their activity. A low calcination temperature will result in incomplete carbonization and a low amount of BTMC in the catalysts, thus decreasing the catalytic activity (Figs. S56-S63). In contrast, a high calcination temperature leads to the destruction of the structure and the increase of particle size, thus giving low electrocatalytic activity (Figs. S56-S63).

3.4. Electrocatalytic overall water splitting performance

Based on good performance of the Co$_6$Mo$_6$C/MoC/Co catalysts for HER and OER, we further employ Co-Mo-0.005–6N and Co-Mo-0.125–6N catalysts as anode and cathode, respectively, for overall water splitting (Fig. 9a). As shown in Fig. 9b, the cell voltage required for Co-Mo-0.005–6N‖Co-Mo-0.125–6N is only 1.53 V to achieve a current density of 10 mA cm^{-2}, which is better than Pt/C‖RuO$_2$ cell (1.61 V) and most reported electrocatalysts (Table S5). In addition, the chronoamperometric curve (Fig. 9b, inset) shows negligible degradation after continuous 96 h operation, indicating the excellent stability of Co-Mo-0.125–6N‖Co-Mo-0.005–6N for overall water splitting. Combined with commercial solar panels, a solar-assisted water splitting device is assembled. As displayed in Fig. 9c and d, the electrolyzer can be driven by a 1.5 V solar cell with obvious H$_2$ and O$_2$ bubbles at the surfaces of both electrodes, indicating its potential to convert low-voltage electricity generated from solar energy into chemical energy. Further, the actual amount of hydrogen and oxygen gas was collected and measured using a home-made electrolytic cell device by drainage method (Fig. 9e). Continuous gas bubbles were observed at cathode and anode during the chronoamperometric measurement (Fig. 9 f). By recording the gas volume at a series of operating time, the calculated volume ratio of H$_2$ and O$_2$ is about 2.17:1, approaching the theoretical value in water electrolysis (Figs. 9g-h and S64). Based on the above results, the calculated faradaic efficiency (FE) of HER and OER is about 100% and 92%, respectively (Fig. 9i).

4. Conclusions

In summary, we developed a simple method toward bimetallic TMICs with tunable metal ratio (Co$_6$Mo$_6$C/MoC/Co heterojunction electrocatalysts) for efficient HER and OER. The components of the catalysts can be well adjusted, which can tune the electronic structure and optimize the adsorption/desorption of H* and water, enhancing the intrinsic activity toward HER and OER. As a result, the Co$_6$Mo$_6$C/MoC/Co electrocatalysts exhibit good performance with low overpotentials of 52 and 223 mV at 10 mA cm^{-2} for HER and OER, respectively. The electrolyzer assembled by the easily coupled Co$_6$Mo$_6$C/MoC/Co catalysts can be driven by a solar panel to achieve continuous hydrogen evolution. The study provides a two-way street in which tuning metal ratio can modulate electronic structure in different directions to facilitate cathodic reaction and anodic reaction for realizing the improved efficiency of the overall reaction.

CRediT authorship contribution statement

Xinhui Zhang: Investigation, Writing – original draft, Writing – review & editing. **Aiping Wu:** Investigation, Methodology,
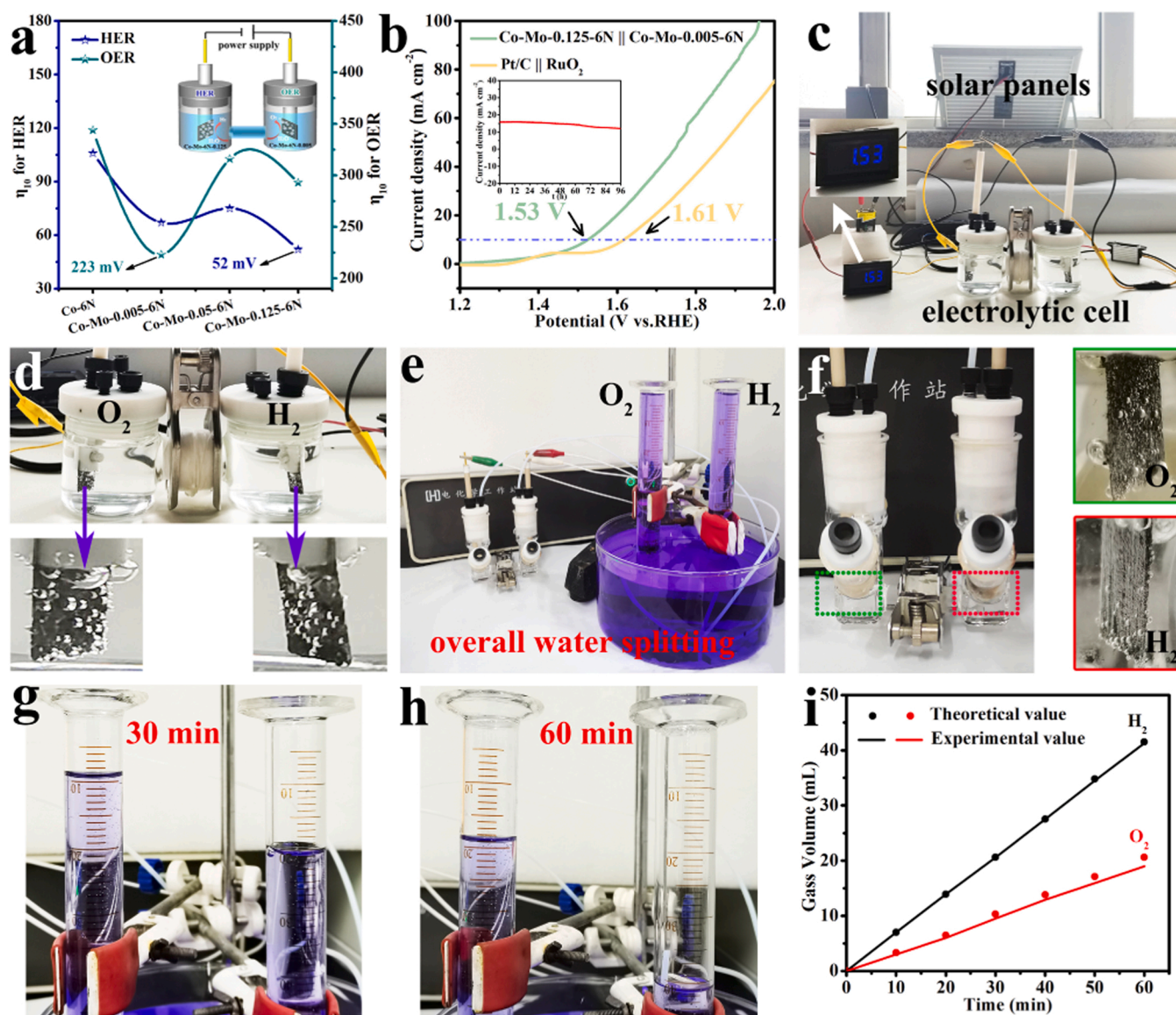
Fig. 9. (a) Performance plots of the synthesized samples, and schematic electrolytic cell of using the samples with the best HER and OER performance as electrodes for overall water splitting; (b) Polarization curves for Co-Mo-0.125–6N‖Co-Mo-0.005–6N and Pt/C‖RuO$_2$ in 1 M KOH, Inset: I-t curve of Co-Mo-0.125–6N‖Co-Mo-0.005–6N for 96 h; (c) Digital photograph of solar panel assisted water splitting device; (d) the magnified photos of electrolyzer. Inset: magnified pictures of the electrodes; (e) A drainage setup for collecting hydrogen and oxygen produced; (f) Generator for preparing hydrogen and oxygen, the inset shows the schematic diagram about the evolution of H$_2$ and O$_2$; (g,h) The volume of gas produced in 30 and 60 min; (i) volume of collected H$_2$ and O$_2$ versus time.

Conceptualization, Writing – original draft, Writing – review & editing. **Dongxu Wang:** Investigation, Formal analysis. **Yanqing Jiao:** Investigation, Formal analysis. **Haijing Yan:** Investigation, Formal analysis. **Chengxu Jin:** Investigation, Formal analysis. **Ying Xie:** Investigation, Methodology, Resources. **Chungui Tian:** Supervision, Conceptualization, Writing – original draft, Writing – review & editing.

Declaration of Competing Interest

The authors declare that they have no known competing financial interests or personal relationships that could have appeared to influence the work reported in this paper.

Data availability

Data will be made available on request.

Appendix A. Supporting information

Supplementary data associated with this article can be found in the online version at doi:10.1016/j.apcatb.2023.122474.

References

[1] Y. Gu, A. Wu, Y. Jiao, H. Zheng, X. Wang, Y. Xie, L. Wang, C. Tian, H. Fu, Two-dimensional porous molybdenum phosphide/nitride heterojunction nanosheets for pH-universal hydrogen evolution reaction, Angew. Chem. Int. Ed. 60 (2021) 6673–6681, https://doi.org/10.1002/anie.202016102.

[2] H.S. Jadhav, H.A. Bandal, S. Ramakrishna, H. Kim, Critical review, recent updates on zeolitic imidazolate framework-67 (ZIF-67) and its derivatives for electrochemical water splitting, Adv. Mater. 34 (2022), 2107072, https://doi.org/10.1002/adma.202107072.

[3] Y. Li, X. Wei, L. Chen, J. Shi, Electrocatalytic hydrogen production trilogy, Angew. Chem. Int. Ed. 60 (2021) 19550–19571, https://doi.org/10.1002/anie.202009854.

[4] N.K. Oh, J. Seo, S. Lee, H.J. Kim, U. Kim, J. Lee, Y.K. Han, H. Park, Highly efficient and robust noble-metal free bifunctional water electrolysis catalyst achieved via complementary charge transfer, Nat. Commun. 12 (2021) 4606, https://doi.org/10.1038/s41467-021-24829-8.

[5] S. Hou, W. Li, S. Watzele, R.M. Kluge, S. Xue, S. Yin, X. Jiang, M. Doblinger, A. Welle, B. Garlyyev, M. Koch, P. Muller-Buschbaum, C. Woll, A.S. Bandarenka, R. A. Fischer, Metamorphosis of heterostructured surface-mounted metal-organic frameworks yielding record oxygen evolution mass activities, Adv. Mater. 33 (2021), e2103218, https://doi.org/10.1002/adma.202103218.

[6] L. Huang, R. Yao, X. Wang, S. Sun, X. Zhu, X. Liu, M.G. Kim, J. Lian, F. Liu, Y. Li, H. Zong, S. Han, X. Ding, In situ phosphating of Zn-doped bimetallic skeletons as a versatile electrocatalyst for water splitting, Energy Environ. Sci. 15 (2022) 2425–2434, https://doi.org/10.1039/d1ee02764f.

[7] M. Yu, E. Budiyanto, H. Tuysuz, Principles of water electrolysis and recent progress in cobalt-, nickel-, and iron-based oxides for the oxygen evolution reaction, Angew. Chem. Int. Ed. 61 (2022), e202103824, https://doi.org/10.1002/anie.202103824.

[8] Y. Chen, J. Wang, Z. Yu, Y. Hou, R. Jiang, M. Wang, J. Huang, J. Chen, Y. Zhang, H. Zhu, Functional group scission-induced lattice strain in chiral macromolecular metal-organic framework arrays for electrocatalytic overall water splitting, Appl. Catal. B Environ. 307 (2022), 121151, https://doi.org/10.1016/j.apcatb.2022.121151.

[9] E. Lee, H. Park, H. Joo, B.P.T. Fokwa, Unexpected correlation between boron chain condensation and hydrogen evolution reaction (HER) activity in highly active vanadium borides: Enabling predictions, Angew. Chem. Int. Ed. 59 (2020) 11774–11778, https://doi.org/10.1002/anie.202000154.

[10] H. Wang, J. Li, K. Li, Y. Lin, J. Chen, L. Gao, V. Nicolosi, X. Xiao, J.M. Lee, Transition metal nitrides for electrochemical energy applications, Chem. Soc. Rev. 50 (2021) 1354–1390, https://doi.org/10.1039/d0cs00415d.

[11] S. Zhao, L. Yin, L. Deng, J. Song, Y.M. Chang, F. Hu, H. Wang, H.Y. Chen, L. Li, S. Peng, Inheritable organic-inorganic hybrid interfaces with π-d electron coupling for robust electrocatalytic hydrogen evolution at high-current-densities, Adv. Funct. Mater. (2022), 2211576, https://doi.org/10.1002/adfm.202211576.

[12] Y. Lin, Z. Yang, Z. Liu, J. Zheng, M. Feng, Y. Zhi, L. Lu, M. Liao, W. Liu, D. Ma, Q. Han, H. Cheng, Q. Zeng, Z. Yuan, B. Yan, Y. Zeng, J. Ye, Dual-functional carbon-doped polysilicon films for passivating contact solar cells: regulating physical contacts while promoting photoelectrical properties, Energy Environ. Sci. 14 (2021) 6406–6418, https://doi.org/10.1039/d1ee02011k.

[13] Q. Gao, W. Zhang, Z. Shi, L. Yang, Y. Tang, Structural design and electronic modulation of transition-metal-carbide electrocatalysts toward efficient hydrogen evolution, Adv. Mater. 31 (2019), e1802880, https://doi.org/10.1002/adma.201802880.

[14] J. Wang, H. Kong, J. Zhang, Y. Hao, Z. Shao, F. Ciucci, Carbon-based electrocatalysts for sustainable energy applications, Prog. Mater. Sci. 116 (2021), 100717, https://doi.org/10.1016/j.pmatsci.2020.100717.

[15] F. Hu, D. Yu, M. Ye, H. Wang, Y. Hao, L. Wang, L. Li, X. Han, S. Peng, Lattice-matching formed mesoporous transition metal oxide heterostructures advance water splitting by active Fe-O-Cu bridges, Adv. Energy Mater. 12 (2022), 2200067, https://doi.org/10.1002/aenm.202200067.

[16] H. Guo, A. Wu, Y. Xie, H. Yan, D. Wang, L. Wang, C. Tian, 2D porous molybdenum nitride/cobalt nitride heterojunction nanosheets with interfacial electron redistribution for effective electrocatalytic overall water splitting, J. Mater. Chem. A 9 (2021) 8620–8629, https://doi.org/10.1039/d0ta11997k.

[17] M. Guo, S. Song, S. Zhang, Y. Yan, K. Zhan, J. Yang, B. Zhao, Fe-doped Ni–Co phosphide nanoplates with planar defects as an efficient bifunctional electrocatalyst for overall water splitting, ACS Sustain. Chem. Eng. 8 (2020) 7436–7444, https://doi.org/10.1021/acssuschemeng.0c01467.

[18] H. Yan, Y. Xie, A. Wu, Z. Cai, L. Wang, C. Tian, X. Zhang, H. Fu, Anion-modulated HER and OER activities of 3D Ni-V-based interstitial compound heterojunctions for high-efficiency and stable overall water splitting, Adv. Mater. 31 (2019), e1901174, https://doi.org/10.1002/adma.201901174.

[19] R. Li, Y. Li, P. Yang, P. Ren, D. Wang, X. Lu, R. Xu, Y. Li, J. Xue, J. Zhang, M. An, J. Ma, B. Wang, H. Liu, S. Dou, Synergistic interface engineering and structural optimization of non-noble metal telluride-nitride electrocatalysts for sustainably overall seawater electrolysis, Appl. Catal. B Environ. 318 (2022), 121834, https://doi.org/10.1016/j.apcatb.2022.121834.

[20] D. Tian, S.R. Denny, K. Li, H. Wang, S. Kattel, J.G. Chen, Density functional theory studies of transition metal carbides and nitrides as electrocatalysts, Chem. Soc. Rev. 50 (2021) 12338–12376, https://doi.org/10.1039/d1cs00590a.

[21] A. Zhang, Y. Liang, H. Zhang, Z. Geng, J. Zeng, Doping regulation in transition metal compounds for electrocatalysis, Chem. Soc. Rev. 50 (2021) 9817–9844, https://doi.org/10.1039/d1cs00330e.

[22] Y.-Q. Jiao, H.-J. Yan, C.-G. Tian, H.-G. Fu, Structure engineering and electronic modulation of transition metal interstitial compounds for electrocatalytic water splitting, Acc. Mater. Res (2022), https://doi.org/10.1021/accountsmr.2c00188.

[23] D.S. Baek, J. Lee, J. Kim, S.H. Joo, Metastable phase-controlled synthesis of mesoporous molybdenum carbides for efficient alkaline hydrogen evolution, ACS Catal. 12 (2022) 7415–7426, https://doi.org/10.1021/acscatal.2c01772.

[24] Z. Chen, Y. Xu, D. Ding, G. Song, X. Gan, H. Li, W. Wei, J. Chen, Z. Li, Z. Gong, X. Dong, C. Zhu, N. Yang, J. Ma, R. Gao, D. Luo, S. Cong, L. Wang, Z. Zhao, Y. Cui, Thermal migration towards constructing W-W dual-sites for boosted alkaline hydrogen evolution reaction, Nat. Commun. 13 (2022) 763, https://doi.org/10.1038/s41467-022-28413-6.

[25] R. Hu, H. Jiang, J. Xian, S. Mi, L. Wei, G. Fang, J. Guo, S. Xu, Z. Liu, H. Jin, W. Xu, J. Wan, Microwave-pulse sugar-blowing assisted synthesis of 2D transition metal carbides for sustainable hydrogen evolution, Appl. Catal. B Environ. 317 (2022), 121728, https://doi.org/10.1016/j.apcatb.2022.121728.

[26] Y. Feng, R. Wang, P. Dong, X. Wang, W. Feng, J. Chen, L. Cao, L. Feng, C. He, J. Huang, Enhanced electrocatalytic activity of nickel cobalt phosphide nanoparticles anchored on porous N-doped fullerene nanorod for efficient overall water splitting, ACS Appl. Mater. Interfaces 13 (2021) 48949–48961, https://doi.org/10.1021/acsami.1c16546.

[27] L. Ji, J. Wang, X. Teng, T.J. Meyer, Z. Chen, CoP nanoframes as bifunctional electrocatalysts for efficient overall water splitting, ACS Catal. 10 (2019) 412–419, https://doi.org/10.1021/acscatal.9b03623.

[28] T. Ling, M. Jaroniec, S.Z. Qiao, Recent progress in engineering the atomic and electronic structure of electrocatalysts via cation exchange reactions, Adv. Mater. 32 (2020), e2001866, https://doi.org/10.1002/adma.202001866.

[29] L. Tao, Y. Wang, Y. Zou, N. Zhang, Y. Zhang, Y. Wu, Y. Wang, R. Chen, S. Wang, Charge transfer modulated activity of carbon-based electrocatalysts, Adv. Energy Mater. 10 (2020), 1901227, https://doi.org/10.1002/aenm.201901227.

[30] Z.P. Wu, H. Zhang, S. Zuo, Y. Wang, S.L. Zhang, J. Zhang, S.Q. Zang, X.W.D. Lou, Manipulating the local coordination and electronic structures for efficient electrocatalytic oxygen evolution, Adv. Mater. 33 (2021), e2103004, https://doi.org/10.1002/adma.202103004.

[31] L. Wang, L. Song, Z. Yang, Y.M. Chang, F. Hu, L. Li, L. Li, H.Y. Chen, S. Peng, Electronic modulation of metal-organic frameworks by interfacial bridging for efficient pH-universal hydrogen evolution, Adv. Funct. Mater. (2022), 2210322, https://doi.org/10.1002/adfm.202210322.

[32] L. Guo, J. Wang, X. Teng, Y. Liu, X. He, Z. Chen, A novel bimetallic nickel-molybdenum carbide nanowire array for efficient hydrogen evolution, ChemSusChem 11 (2018) 2717–2723, https://doi.org/10.1002/cssc.201801110.

[33] X. Li, L. Yang, T. Su, X. Wang, C. Sun, Z. Su, Graphene-coated hybrid electrocatalysts derived from bimetallic metal–organic frameworks for efficient hydrogen generation, J. Mater. Chem. A 5 (2017) 5000–5006, https://doi.org/10.1039/c6ta10405c.

[34] M.Y. Zu, C. Wang, L. Zhang, L.R. Zheng, H.G. Yang, Reconstructing bimetallic carbide Mo$_6$Ni$_6$C for carbon interconnected MoNi alloys to boost oxygen evolution electrocatalysis, Mater. Horiz. 6 (2019) 115–121, https://doi.org/10.1039/c8mh00664d.

[35] J. Su, G. Xia, R. Li, Y. Yang, J. Chen, R. Shi, P. Jiang, Q. Chen, Co$_3$ZnC/Co nano heterojunctions encapsulated in nitrogen-doped graphene layers derived from PBAs as highly efficient bi-functional electrocatalysts for both OER and ORR, J. Mater. Chem. A 4 (2016) 9204–9212, https://doi.org/10.1039/c6ta00945j.

[36] Y.J. Tang, C.H. Liu, W. Huang, X.L. Wang, L.Z. Dong, S.L. Li, Y.Q. Lan, Bimetallic carbides-based nanocomposite as superior electrocatalyst for oxygen evolution reaction, ACS Appl. Mater. Interfaces 9 (2017) 16977–16985, https://doi.org/10.1021/acsami.7b01096.

[37] J. Chen, B. Ren, H. Cui, C. Wang, Constructing pure phase tungsten-based bimetallic carbide nanosheet as an efficient bifunctional electrocatalyst for overall water splitting, Small 16 (2020), e1907556, https://doi.org/10.1002/smll.201907556.

[38] L. Qiao, A. Zhu, W. Zeng, R. Dong, P. Tan, Z. Ding, P. Gao, S. Wang, J. Pan, Achieving electronic structure reconfiguration in metallic carbides for robust electrochemical water splitting, J. Mater. Chem. A 8 (2020) 2453–2462, https://doi.org/10.1039/c9ta10682k.

[39] S. Sanati, A. Morsali, H. García, First-row transition metal-based materials derived from bimetallic metal–organic frameworks as highly efficient electrocatalysts for electrochemical water splitting, Energy Environ. Sci. 15 (2022) 3119, https://doi.org/10.1039/d1ee03614a.

[40] M. Yao, B. Wang, N. Wang, S. Komarneni, Y. Chen, J. Wang, X. Niu, W. Hu, Self-supported composite of (Ni,Co)$_3$C mesoporous nanosheets/N-doped carbon as a flexible electrocatalyst for pH-universal hydrogen evolution, ACS Sustain. Chem. Eng. 8 (2020) 5287–5295, https://doi.org/10.1021/acssuschemeng.0c00268.

[41] C. Chen, A. Wu, H. Yan, Y. Xiao, C. Tian, H. Fu, Trapping [PMo$_{12}$O$_{40}$]$^{3-}$ clusters into pre-synthesized ZIF-67 toward Mo$_x$Co$_x$C particles confined in uniform carbon polyhedrons for efficient overall water splitting, Chem. Sci. 9 (2018) 4746–4755, https://doi.org/10.1039/c8sc01454j.

[42] P. He, X.Y. Yu, X.W. Lou, Carbon-incorporated nickel-cobalt mixed metal phosphide nanoboxes with enhanced electrocatalytic activity for oxygen evolution, Angew. Chem. Int. Ed. 56 (2017) 3897–3900, https://doi.org/10.1002/anie.201612635.

[43] Y. Lu, L. Yu, M. Wu, Y. Wang, X.W.D. Lou, Construction of complex Co$_3$O$_4$@ Co$_3$V$_2$O$_8$ hollow structures from metal-organic frameworks with enhanced lithium storage properties, Adv. Mater. 30 (2018), 1702875, https://doi.org/10.1002/adma.201702875.

[44] T. Qiu, S. Gao, Z. Liang, D.G. Wang, H. Tabassum, R. Zhong, R. Zou, Pristine hollow metal-organic frameworks: design, synthesis and application, Angew. Chem. Int. Ed. 60 (2021) 17314–17336, https://doi.org/10.1002/anie.202012699.

[45] R. Zhao, Z. Liang, R. Zou, Q. Xu, Metal-organic frameworks for batteries, Joule 2 (2018) 2235–2259, https://doi.org/10.1016/j.joule.2018.09.019.

[46] R. Yu, X.-F. Kuang, X.-Y. Wu, C.-Z. Lu, J.P. Donahue, Stabilization and immobilization of polyoxometalates in porous coordination polymers through host-guest interactions, Coord. Chem. Rev. 253 (2009) 2872–2890, https://doi.org/10.1016/j.ccr.2009.07.003.

[47] Y. Sun, X. Zuo, S.K.R.S. Sankaranarayanan, S. Peng, B. Narayanan, G. Kamath, Quantitative 3D evolution of colloidal nanoparticle oxidation in solution (https://), Science 356 (2017) 303–307, https://doi.org/10.1126/science.aaf6792.

[48] T. He, X. Xu, B. Ni, H. Lin, C. Li, W. Hu, X. Wang, Metal-organic framework based microcapsules, Angew. Chem. Int. Ed. 57 (2018) 10148–10152, https://doi.org/10.1002/anie.201804792.

[49] B. Zhao, N. Wu, S. Yao, Y. Yao, Y. Lian, B. Li, Z. Zeng, J. Liu, Molybdenum carbide/cobalt composite nanorods via a "mofs plus mofs" strategy for high-efficiency microwave absorption, ACS Appl. Nano Mater. 5 (2022) 18697–18707, https://doi.org/10.1021/acsanm.2c04460.

[50] Y. Li, Z. Yin, M. Cui, S. Chen, T. Ma, Bimetallic cobalt molybdenum carbide–cobalt composites as superior bifunctional oxygen electrocatalysts for Zn–air batteries, Mater. Today Energy 18 (2020), 100565, https://doi.org/10.1016/j.mtener.2020.100565.

[51] S. Chen, X. Liu, H. Sun, Z. Cao, J. Xiong, Y. Li, Facile synthesis of carbon coated cobalt-cobalt molybdenum carbide as advanced bifunctional oxygen electrocatalyst for rechargeable Zn-air battery, J. Alloy. Compd. 897 (2022), 163203, https://doi.org/10.1016/j.jallcom.2021.163203.

[52] L. Qiu, L. Jiang, Z. Ye, Y. Liu, T. Cen, X. Peng, D. Yuan, Phosphorus-doped Co₃Mo₃C/Co/CNFs hybrid: A remarkable electrocatalyst for hydrogen evolution reaction, Electrochim. Acta 325 (2019) 134962, https://doi.org/10.1016/j.electacta.2019.134962.

[53] S. Wang, Y. Cao, W. Jia, Z. Lu, D. Jia, A cage-confinement strategy to fabricate Pt-Mo₆Co₆C heterojunction for highly efficient pH-universal hydrogen evolution, Appl. Catal. B Environ. 298 (2021) 120579, https://doi.org/10.1016/j.apcatb.2021.120579.

[54] M. Kuang, Q. Wang, P. Han, G. Zheng, Cu, Co-embedded N-enriched mesoporous carbon for efficient oxygen reduction and hydrogen evolution reactions, Adv. Energy Mater. 7 (2017), 1700193, https://doi.org/10.1002/aenm.201700193.

[55] C. He, J. Tao, Three-dimensional hollow porous Co₆Mo₆C nanoframe as an highly active and durable electrocatalyst for water splitting, J. Catal. 347 (2017) 63–71, https://doi.org/10.1016/j.jcat.2017.01.007.

[56] Y. Liu, G. Yu, G.D. Li, Y. Sun, T. Asefa, W. Chen, X. Zou, Coupling Mo₂C with nitrogen-rich nanocarbon leads to efficient hydrogen-evolution electrocatalytic sites, Angew. Chem. Int. Ed. 54 (2015) 10752–10757, https://doi.org/10.1002/anie.201504376.

[57] L. Wang, X. Bai, B. Wen, Z. Du, Y. Lin, Honeycomb-like Co/C composites derived from hierarchically nanoporous ZIF-67 as a lightweight and highly efficient microwave absorber, Compos Part B Eng. 166 (2019) 464–471, https://doi.org/10.1016/j.compositesb.2019.02.054.

[58] Z. Shi, Y. Wang, H. Lin, H. Zhang, M. Shen, S. Xie, Y. Zhang, Q. Gao, Y. Tang, Porous nanomoc@graphite shell derived from a MOFs-directed strategy: An efficient electrocatalyst for the hydrogen evolution reaction, J. Mater. Chem. A 4 (2016) 6006–6013, https://doi.org/10.1039/c6ta01900e.

[59] W. Liu, X. Wang, F. Wang, K. Du, Z. Zhang, Y. Guo, H. Yin, D. Wang, A durable and pH-universal self-standing MoC-Mo₂C heterojunction electrode for efficient hydrogen evolution reaction, Nat. Commun. 12 (2021) 6776, https://doi.org/10.1038/s41467-021-27118-6.

[60] L. Zhang, Y. Zhu, Z. Nie, Z. Li, Y. Ye, L. Li, J. Hong, Z. Bi, Y. Zhou, G. Hu, Co/MoC nanoparticles embedded in carbon nanoboxes as robust trifunctional electrocatalysts for a Zn-Air battery and water electrocatalysis, ACS Nano 15 (2021) 13399–13414, https://doi.org/10.1021/acsnano.1c03766.

[61] C. Wan, Y.N. Regmi, B.M. Leonard, Multiple phases of molybdenum carbide as electrocatalysts for the hydrogen evolution reaction, Angew. Chem. Int. Ed. 53 (2014) 6407–6410, https://doi.org/10.1002/anie.201402998.

[62] X. Feng, X. Bo, L. Guo, An advanced hollow bimetallic carbide/nitrogen-doped carbon nanotube for efficient catalysis of oxygen reduction and hydrogen evolution

and oxygen evolution reaction, J. Colloid Interface Sci. 575 (2020) 69–77, https://doi.org/10.1016/j.jcis.2020.04.093.

[63] W. Wang, L. Huai, S. Wu, J. Shan, J. Zhu, Z. Liu, L. Yue, Y. Li, Ultrahigh-volumetric-energy-density lithium-sulfur batteries with lean electrolyte enabled by cobalt-doped MoSe₂/Ti₃C₂Tₓ mxene bifunctional catalyst, ACS Nano 15 (2021) 11619–11633, https://doi.org/10.1021/acsnano.1c02047.

[64] H. Ma, Z. Chen, Z. Wang, C.V. Singh, Q. Jiang, Interface engineering of Co/CoMoN/NF heterostructures for high-performance electrochemical overall water splitting, Adv. Sci. 9 (2022), e2105313, https://doi.org/10.1002/advs.202105313.

[65] A. Wu, Y. Gu, B. Yang, H. Wu, H. Yan, Y. Jiao, D. Wang, C. Tian, H. Fu, Porous cobalt/tungsten nitride polyhedra as efficient bifunctional electrocatalysts for overall water splitting, J. Mater. Chem. A 8 (2020) 22938–22946, https://doi.org/10.1039/d0ta09620b.

[66] C. Li, H. Jang, S. Liu, M.G. Kim, L. Hou, X. Liu, J. Cho, P and Mo dual doped Ru ultrasmall nanoclusters embedded in P-doped porous carbon toward efficient hydrogen evolution reaction, Adv. Energy Mater. 12 (2022), 2200029, https://doi.org/10.1002/aenm.202200029.

[67] H. Yan, C. Tian, L. Wang, A. Wu, M. Meng, L. Zhao, H. Fu, Phosphorus-modified tungsten nitride/reduced graphene oxide as a high-performance, non-noble-metal electrocatalyst for the hydrogen evolution reaction, Angew. Chem. Int. Ed. 54 (2015) 6325–6329, https://doi.org/10.1002/anie.201501419.

[68] N. Li, J. Liu, B.X. Dong, Y.Q. Lan, Polyoxometalate-based compounds for photo- and electrocatalytic applications, Angew. Chem. Int. Ed. 59 (2020) 20779–20793, https://doi.org/10.1002/anie.202008054.

[69] H.F. Wang, L. Chen, H. Pang, S. Kaskel, Q. Xu, MOF-derived electrocatalysts for oxygen reduction, oxygen evolution and hydrogen evolution reactions, Chem. Soc. Rev. 49 (2020) 1414–1448, https://doi.org/10.1039/c9cs00906j.

[70] C.-Z. Yuan, K.S. Hui, H. Yin, S. Zhu, J. Zhang, X.-L. Wu, X. Hong, W. Zhou, X. Fan, F. Bin, F. Chen, K.N. Hui, Regulating intrinsic electronic structures of transition-metal-based catalysts and the potential applications for electrocatalytic water splitting, ACS Mater. Lett. 3 (2021) 752–780, https://doi.org/10.1021/acsmaterialslett.0c00549.

[71] Y. Huang, L.W. Jiang, B.Y. Shi, K.M. Ryan, J.J. Wang, Highly efficient oxygen evolution reaction enabled by phosphorus doping of the Fe electronic structure in iron-nickel selenide nanosheets, Adv. Sci. 8 (2021), e2101775, https://doi.org/10.1002/advs.202101775.

[72] X. Wang, X. Zhou, C. Li, H. Yao, C. Zhang, J. Zhou, R. Xu, L. Chu, H. Wang, M. Gu, H. Jiang, M. Huang, Asymmetric Co-N3P1 trifunctional catalyst with tailored electronic structures enabling boosted activities and corrosion resistance in an uninterrupted seawater splitting system, Adv. Mater. 34 (2022), e2204021, https://doi.org/10.1002/adma.202204021.

[73] X. Han, X. Ling, Y. Wang, Y. Ma, C. Zhong, W. Hu, Y. Deng, Generation of nanoparticle, atomic-cluster, and single-atom cobalt catalysts from zeolitic imidazole frameworks by spatial isolation and their use in zinc–air batteries, Angew. Chem. Int. Ed. 58 (2019) 5359–5364, https://doi.org/10.1002/anie.201901109.

[74] H. Zhang, D. Guan, Z. Hu, Y.-C. Huang, X. Wu, J. Dai, C.-L. Dong, X. Xu, H.-J. Lin, C.-T. Chen, W. Zhou, Z. Shao, Exceptional lattice-oxygen participation on artificially controllable electrochemistry-induced crystalline-amorphous phase to boost oxygen-evolving performance, Appl. Catal. B Environ. 297 (2021), 120484, https://doi.org/10.1016/j.apcatb.2021.120484.

[75] R. Zhang, Z. Wei, G. Ye, G. Chen, J. Miao, X. Zhou, X. Zhu, X. Cao, X. Sun, "D-Electron Complementation" induced V-Co phosphide for efficient overall water splitting, Adv. Energy Mater. 11 (2021), 2101758, https://doi.org/10.1002/aenm.202101758.

[76] L. Wang, Y. Hao, L. Deng, F. Hu, S. Zhao, L. Li, S. Peng, Rapid complete reconfiguration induced actual active species for industrial hydrogen evolution reaction, Nat. Commun. 13 (2022) 5785, https://doi.org/10.1038/s41467-022-33590-5.

[77] S. Li, Y. Gao, N. Li, L. Ge, X. Bu, P. Feng, Transition metal-based bimetallic MOFs and MOF-derived catalysts for electrochemical oxygen evolution reaction, Energy Environ. Sci. 14 (2021) 1897–1927, https://doi.org/10.1039/d0ee03697h.